⌘ *Author's Choice*

THE JOURNAL OF BIOLOGICAL CHEMISTRY VOL. 287, NO. 45, pp. 37715–37731, November 2, 2012

Biophysical Analysis of Kindlin-3 Reveals an Elongated Conformation and Maps Integrin Binding to the Membrane-distal β-Subunit NP*X*Y Motif

Received for publication, August 31, 2012, and in revised form, September 17, 2012 Published, JBC Papers in Press, September 18, 2012, DOI 10.1074/jbc.M112.415208

Luke A. Yates[‡1], **Anna K. Füzéry**[§2], **Roman Bonet**[§3], **Iain D. Campbell**[§], **and Robert J. C. Gilbert**[‡4]

From the [‡]*Division of Structural Biology, Wellcome Trust Centre for Human Genetics, Roosevelt Drive, University of Oxford, Oxford OX3 7BN, United Kingdom and the* [§]*Department of Biochemistry, South Parks Road, University of Oxford, Oxford OX1 3QU, United Kingdom*

Background: Kindlins are essential co-activators of integrins.
Results: Kindlin-3 has an elongated structure and forms a ternary complex with the Talin head and integrin β-tails. The Kindlin-3-tail interface involves a membrane-distal NP*X*Y motif on the tail.
Conclusion: New information about the conformation and interactions of Kindlin-3 has been obtained.
Significance: The solution structure and protein/protein interactions of Kindlin-3 give insight into its role.

Kindlin-3, a 75-kDa protein, has been shown to be critical for hemostasis, immunity, and bone metabolism via its role in integrin activation. The Kindlin family is hallmarked by a FERM domain comprised of F1, F2, and F3 subdomains together with an N-terminal F0 domain and a pleckstrin homology domain inserted in the F2 domain. Recombinant Kindlin-3 was cloned, expressed, and purified, and its domain organization was studied by x-ray scattering and other techniques to reveal an extended conformation. This unusual elongated structure is similar to that found in the paralogue Talin head domain. Analytical ultracentrifugation experiments indicated that Kindlin-3 forms a ternary complex with the Talin and β-integrin cytoplasmic tails. NMR showed that Kindlin-3 specifically recognizes the membrane-distal tail NP*X*Y motif in both the β_{1A} and β_{1D} isoforms, although the interaction is stronger with β_{1A}. An upstream Ser/Thr cluster in the tails also plays a critical role. Overall these data support current biological, clinical, and mutational data on Kindlin-3/β-tail binding and provide novel insights into the overall conformation and interactions of Kindlin-3.

Integrin-mediated cell adhesion connects the cell surface to the extracellular matrix in higher eukaryotes. It is a critical and common process in a plethora of physiological phenomena, including tissue integrity, embryogenesis, bone metabolism, hemostasis, and immunity. Integrin heterodimers form one of the most important cell-extracellular matrix receptors, and tight regulation of integrin ligand affinity is crucial for cell survival. The bi-directional signaling properties of integrins give them added interest (1); key steps in their intracellular activation involve binding of Talin and Kindlin to the cytoplasmic tails of the integrin β-subunits (2, 3).

The Kindlin family of proteins has recently emerged as a crucial component of focal adhesion assembly. There is evidence that, alongside Talin, they are co-activators of integrins (4). In mammals there are three Kindlin isoforms, Kindlins 1, 2, and 3, all multidomain cytoplasmic proteins of ~75 kDa. The domain structure of Kindlins and their homology with the Talin head domain are illustrated in Fig. 1. Like Talin they have F0, F1, F2, and F3 subdomains but in addition have a pleckstrin homology (PH)[5] domain inserted in the F2 domain. The F1, F2, and F3 domains have homology with FERM (4.1 band, ezrin, radixin, moesin) domains (5–7). There is also a long loop inserted into the F1 domain of Kindlins that is predicted to be unfolded (8) and which, in Kindlin-3, contains 109 residues.

The three mammalian Kindlins display tissue-specific expression patterns. Kindlin-1 is found primarily in the epidermis and, to a lesser extent, the colon, stomach, and kidneys (9). Kindlin-2 is ubiquitously expressed but is concentrated in striated and smooth muscle (9). Kindlin-3 was considered to be exclusively expressed in hematopoietic tissues (9) but it has also been found recently in endothelial tissues (10).

Kindlin-3 was first identified during screening for B-cell-specific plasma membrane proteins in chronic lymphocytic leukemia (11). It has significant homology with Kindlin-1, which is mutated in Kindler syndrome (7). Kindlin-3 knock-out mice suffer from severe bleeding because of inactive platelet integrins and die of anemia (12, 13). Kindlin-3 is involved in podocyte formation in osteoclasts (14) an observation that explains, in part, the observed osteopetrosis found in Kindlin-3-deficient mice and in human LAD-III sufferers (12, 14, 15). Kindlin-3 also appears to have a role in red blood cell function (16).

⌘ *Author's Choice*—Final version full access.

[1] Supported by a Medical Research Council (MRC) graduate studentship.
[2] Supported by Grant U54 GM06434 from the National Institutes of Health-funded Cell Migration Consortium. Present address: Dept. of Pathology, Johns Hopkins University, Baltimore, MD 21287.
[3] Supported by MRC Grant G0900052 1/1.
[4] A Royal Society University Research Fellow. To whom correspondence should be addressed: Div. of Structural Biology, Wellcome Trust Centre for Human Genetics, Roosevelt Dr., OX3 7BN. E-mail: gilbert@strubi.ox.ac.uk.

[5] The abbreviations used are: PH, pleckstrin homology; SAXS, small-angle x-ray scattering; AUC, analytical ultracentrifugation; SEC, size-exclusion chromatography; MWCO, molecular weight cut-off; bis-Tris, 2-[bis(2-hydroxyethyl)amino]-2-(hydroxymethyl)propane-1,3-diol; DLS, dynamic light scattering; MD, membrane-distal.

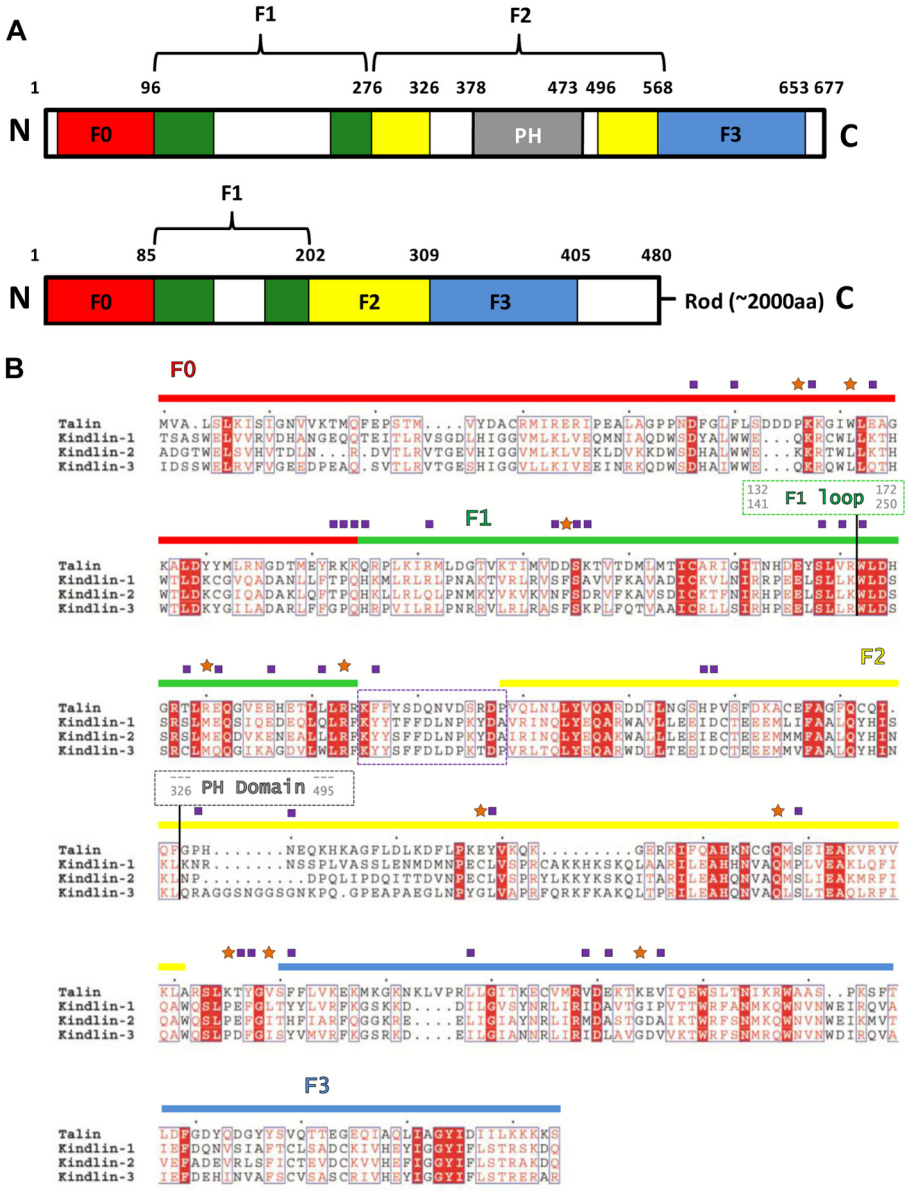

FIGURE 1. **Kindlin protein domain structure and sequence alignment.** *A*, schematic representation of domains from Kindlins (Kindlin-1 numbering) compared with Talin-1. *B*, sequence alignment of the Talin head (residues 1–400) from its crystal structure (PDB code: 3IVF) compared with the FERM domains of mouse Kindlins 1, 2, and 3. The sequences corresponding to the PH domain and the F1 loop regions of the Kindlin sequences were removed prior to sequence alignment. The F1 loop in Talin is missing in the crystal structure and therefore is not present in the sequence. The Talin sequence was aligned with the Kindlin-1 FERM domain, as in Goult *et al.* (48), using ClustalW. The remaining family members were aligned to Kindlin-1 using ClustalW, and the comparison between Talin and the Kindlin family was adjusted by hand. ESPript (57) was used for the final alignment. The domain boundaries are denoted by *colored bars* (as in *A*) above the sequence, and the F1 loop and PH position are *highlighted*. Interfacial residues that are buried in the Talin structure (PDB code: 3IVF) are highlighted (*purple squares*) together with those that mediate an interdomain interaction (*orange stars*).

The phosphotyrosine-binding F3 subdomain of the Talin FERM domain has been shown to bind to an NP*X*Y motif in the cytoplasmic tails of the integrin β-subunit, eliciting the activation of integrins to a high affinity state (17, 18). Pulldown assays have demonstrated that Kindlins are also capable of binding to integrin β-tails (13, 19–21); this binding is also involved in integrin activation *in vivo* (13, 22, 23). Thus, as currently understood, intracellular integrin activation involves both Talin and one of the Kindlins. Whether Talin and Kindlin bind together or separately to the β-tails had been unclear, but evidence that Kindlin-2 forms a ternary complex with β_3 integrin tails and the Talin head domain has been found recently (24). New data on the distinct roles of Kindlin and Talin binding in integrin function have also appeared (25, 26).

There are good structural data showing that Talin recognizes a conserved ("membrane proximal") NP*X*Y motif close to the transmembrane region of the integrin cytoplasmic tail (17, 18). There is no structural information about Kindlin-integrin interactions, but mutational and functional studies indicate that Kindlins bind to a second ("membrane distal") conserved NP*X*Y motif (19). Mutational and biochemical analyses have also suggested that a Ser/Thr-rich region between the two NP*X*Y motifs is critical for Kindlin binding to the β-integrin cytoplasmic tails; this is exemplified by a specific β_3 integrin

S732P mutation that causes Glanzmann thrombasthenia in humans (13, 19).

Here, we describe the expression, using a baculovirus-driven system, of recombinant Kindlin-3 in sufficient quantities to perform a biophysical characterization of the full-length protein. The three-dimensional arrangement of the domains within Kindlin-3 was investigated at low resolution using small-angle x-ray scattering in solution. *Ab initio* envelopes from small-angle x-ray scattering (SAXS) together with other shape estimates in solution reveal that Kindlin-3 is elongated and conformationally similar to Talin but with the prominent addition of the PH domain. Kindlin-3 is also shown to form a ternary complex with the Talin head region and integrin β-tails. Induced changes in NMR spectra show that Kindlin-3 binds directly to the membrane-distal NP*X*Y motif and that the preceding Ser/Thr contributes to this binding.

EXPERIMENTAL PROCEDURES

Kindlin-3 Cloning and Baculovirus Generation—KINLDIN3 cDNA (a kind gift from R. Fässler, Max Planck Institute for Biochemistry, Martinsried, Germany) was amplified using primers 5′-aggagatataccatgATGGCGGGTATGAAGACAGC-3′ and 5′-gtgatggtgatgtttGAAGGCCTCATGGCCTCC-3′ and subsequently cloned into the pOPINE vector (27) encoding a C-terminal hexahistidine tag using the In-fusion enzyme system (Clontech). Plasmid DNA was sequence-verified (Geneservice, Ltd., Oxford, United Kingdom) and purified using standard methods.

Baculovirus generation and insect cell culture maintenance were carried out using standard protocols (28). Briefly, insect cells (*Spodoptera frugiperda*) were co-transfected with recombinant transfer vector, and linearized viral DNA was cultured in Sf900II serum-free media (Invitrogen) supplemented with 100 μg/ml penicillin and 100 μg/ml streptomycin. Virus-containing supernatant was harvested between 6 and 7 days after transfection. Virus was amplified prior to expression using standard methods with a multiplicity of infection of ~0.1. Kindlin-3 expression was achieved by infecting suspension cultures of Sf9 cells in Sf900II supplemented with 100 μg/ml penicillin, 100 μg/ml streptomycin, and 1% FCS with amplified recombinant virus at a multiplicity of infection of 1. Infected cells were harvested 72 h post-infection by centrifugation (1000 × *g*) and stored at −20 °C (or −80 °C for long-term storage).

Recombinant Kindlin-3 Purification for Biophysical Characterization—Frozen baculovirus-infected insect cell pellets expressing recombinant Kindlin-3 were thawed and resuspended with 50 mM NaH_2PO_4, pH 7.4, 500 mM NaCl, 10 mM imidazole, and 1% (v/v) Tween-20 supplemented with EDTA-free protease inhibitor mixture (Roche Applied Science) on ice prior to purification. Complete cell lysis was achieved by incubating the resuspension with the detergent. The recombinant protein was purified using three chromatographic steps after the lysate was clarified by centrifugation at 48,000 × *g* for 1 h at 4 °C. The supernatant was incubated with precharged and equilibrated nickel-Sepharose for 1–2 h at 4 °C. The beads were collected and washed using the batch method; 10 bed volumes of 50 mM NaH_2PO_4, pH 7.4, 500 mM NaCl, and 10 mM imidazole buffer were used to wash the beads. The protein was eluted and collected using 1–3 bed volumes of 50 mM NaH_2PO_4, pH 7.45, and 500 mM NaCl, and 500 mM imidazole. The protein composition of the eluant was assessed by SDS-PAGE and, in the first instance, Western blotting using an anti-His_5 antibody. The eluant containing Kindlin-3 was pooled and buffer-exchanged into 20 mM Tris-HCl, pH 7.5, 200 mM NaCl via a series of dilutions into buffer, and the sample was concentrated using a centrifuge protein concentrator (Millipore) with a 50-kDa molecular weight cut-off (MWCO). The buffer-exchanged protein solution was applied onto a pre-equilibrated HiTrap heparin HP column (5 ml column volume, GE Healthcare). The protein that bound to the column was eluted using a linear NaCl gradient in the same buffer that increased from 200 mM to 1 M NaCl at a rate of 10 mM/ml. The protein composition of the fractionated eluant was assessed by SDS-PAGE and Western blotting, and those containing Kindlin-3 were pooled and concentrated using a centrifuge protein concentrator (Millipore) with a 50-kDa MWCO to 0.5 ml-2 ml sample size. Finally, the concentrated protein was polished and buffer-exchanged using size-exclusion chromatography (SEC). The protein was injected onto a pre-equilibrated Superdex S200 (16/60) or (10/30) (GE Healthcare) in 20 mM Tris-HCl, pH 7.5, 250 mM NaCl, and 1 mM DTT at a rate of 1 ml/min. The eluant from the column was fractionated into 1-ml samples, and the protein elution was monitored using absorbance at 280 nm. The fractions corresponding to a single absorbance peak that resulted from SEC were assessed by SDS-PAGE to determine homogeneity. The purified Kindlin-3 was assessed as >95% pure after this step. The protein was concentrated using a centrifuge protein concentrator (Millipore) with a 50-kDa MWCO to ~15 mg/ml in the gel filtration buffer, flash-frozen in liquid nitrogen, and stored at −80 °C until used. The protein concentration was assessed spectroscopically using a calculated extinction coefficient (ε) of 109,320 M^{-1} cm^{-1} (assuming all Cys residues were reduced).

Preparation of Proteins for NMR—Full-length Kindlin-3 was expressed and purified as described above. The C-terminal His_6 tag was removed prior to size-exclusion chromatography by incubating the purified Kindlin-3 with carboxypeptidaseA-agarose (Sigma) at room temperature for 4 h. Kindlin-3 samples were prepared in buffer at pH 6.1 (10 mM bis-Tris, pH 6.1, 150 mM NaCl, and 2 mM DTT) or at pH 7.0 (20 mM HEPES, pH 7.0, 250 mM NaCl, and 2 mM TCEP).

Full-length β-integrin tails were prepared as reported earlier for the β_3 tail (29). ^{15}N-Labeled tails were expressed in *Escherichia coli* grown in M9 minimal medium supplemented with $^{15}NH_4Cl$. The tails were purified under denaturing conditions (50 mM sodium phosphate, 300 mM NaCl, 8 M urea, and 0.035% β-mercaptoethanol, pH 7.0) by Talon immobilized metal affinity chromatography (Clontech), eluting the polyhistidine-tagged integrin tail in 200 mM imidazole. Further purification was performed by C_{18} reverse phase HPLC using a 5–70% acetonitrile gradient. The polyhistidine tag was removed by overnight cleavage at 4 °C with 3C protease, and the cleaved tails were then purified again by C_{18} reverse phase HPLC.

Analytical Ultracentrifugation (AUC)—AUC was carried out using a Beckman (Palo Alto, CA) Optima XL-I AUC operating in velocity mode, initially with 12-mm sector-shaped centerpieces. Data were collected using 280 nm absorbance optics at a speed of 40,000 rpm with one scan taken every 6 min for a total of 60 scans. The sixth to 30th scans were determined as providing the best resolution of the sedimenting species using initial analyses in SedFit software (30), and the data were analyzed using the $c(s,f/f_0)$ method whereby the distribution of apparent sedimentation coefficients shown by the sample is plotted over a third dimension, the population of species with diffusion coefficients of specific magnitudes as influenced by the frictional ratio of the species. For the initial study of isolated Kindlin-3, a resolution in s of 100 was used and a resolution in f/f_0 of 10. For subsequent studies of mixtures of Kindlin-3, Talin head, and integrin β_{1A} tails, 3-mm path-length cells, the 11th to 60th data scans, and a resolution of $s = 50$ were used. SedFit was also used to compute the hydrodynamic radius, frictional coefficient, and axial ellipsoidal ratio from the AUC data. The frictional coefficient is a unitless quantity that is the ratio between the theoretical behavior of a species, given its weight, partial specific volume, and the experimental conditions, and its actual sedimentation behavior. Plots presented as generated using ProFit software (Uetikon am See, Switzerland) were fitted with a Gaussian function to determine peak centers (which are the species sedimentation coefficients) and peak variances (which are proportional to the diffusion coefficient of the species). All samples were in 20 mM Tris, pH 7.5, 200 mM NaCl.

Dynamic Light Scattering—Dynamic light scattering measurements were conducted on a Protein Solutions DynaPro instrument at 22 °C. Approximately 1 μg of protein was diluted in 20 mM Tris-HCl, pH 7.5, 100 mM NaCl, and 1 mM DTT and centrifuged at 13,000 rpm for 5 min before being placed in the cuvette.

Small-angle X-ray Scattering—SAXS data were collected at EMBL beamline X33 at the DORIS III storage ring, DESY (Hamburg, Germany) (31). The measurements were carried out at 288 K in 20 mM HEPES, pH 7.5, 300 mM NaCl, and 10 mM DTT. A MAR345 image plate at a sample detector distance of 2.43 m and wavelength λ of 0.93 Å, covering the momentum transfer range $0.04 < Q < 5.1$ nm-1 ($Q = 4\pi \sin(\theta)/\lambda$ where 2θ is the scattering angle), was used. The data were processed using standard procedures by the program package PRIMUS (32). SAXS data sets for Kindlin-3 were collected at the following concentrations: 8.7, 4.35, 2.18, and 1.09 mg/ml. The reduced, rotationally averaged SAXS profiles were analyzed using the program GNOM (33). A series of alternative possible maximum dimensions for Kindlin-3 were used to locate a D_{max} defined by the data, which also showed a good fit to the experimental scattering curve. Distance distribution functions $p(r)$ were then used to calculate reconstituted models *ab initio* with the program GASBOR (34). Models calculated starting from the premise of an unknown overall shape were consistently elongated, prolate structures, and therefore a prolate assumption was used in calculating the structures presented. For those samples showing no or limited intermolecular scattering (the two lowest concentrations), 20 models were calculated *ab initio* each time, and then they were sorted in pairwise groups of 10, aligned, averaged, and trimmed to a consensus core structure using the DAMAVER package (35) running its constituent programs DAMSEL, DAMSUP, DAMAVER, and DAMFILT in turn and making use of the route supcomb20 for the alignment procedure, which allows enantiomer testing. This produced two independent scattering bead models from each data set, which were then aligned to each other in CHIMERA (36), converted to CCP4 envelopes using the program GAP (37), and correlated in Fourier space using the program WellMAP.[6] The resolution achieved was estimated based on the 0.5 Fourier shell correlation criterion commonly used in electron microscopy (38) and adapted here for SAXS data. The application of this approach to estimate the resolution of the SAXS structures is consistent with the most conservative such methods, in which two wholly independent models from a data set are compared after calculation (38). The maps were then filtered in WellMAP to the determined resolutions. A theoretical sedimentation coefficient and radius of gyration for the SAXS model was computed using the program HYDRO++, version 10 (39). Plots of $I(Q)$ (intensity of scatter for the Q value range described above) including a Kratky plot (40) were drawn using ProFit software. Fits of atomic models to the scattering envelope were performed using the program VEDA. Fits using SASREF (41) failed, most likely because of the degrees of freedom allowed in fitting three or five rigid bodies to the scattering data. We found the incremental approach of determining an average envelope first and then fitting to it highly effective.

Analytical Gel Filtration—Analytical gel filtration was performed using a Superdex S200 10/30 (GE Healthcare) equilibrated with 10 mM sodium phosphate, pH 7.4, 100 mM NaCl at room temperature. Proteins and mixtures were applied to the column with buffer at a rate of 0.5 ml/min, and the elution profile was recorded using absorbance at 280 nm. All samples were loaded at equivalent molarities, and complex mixtures were combined in a stoichiometric amount except for β_{1A} tail mixtures, where a 3× molar excess was used. All samples that were injected were equivalent in volume. Elution profiles were plotted for analysis using ProFit software.

NMR Spectroscopy—All NMR experiments were recorded at 25 °C on 500 MHz (equipped with a z axis gradient CryoProbe) and 750-MHz spectrometers. All spectra were processed with NMRPipe (42) and analyzed with Sparky (43) and CCPN (44). Samples were prepared in NMR buffer at pH 6.1 and 7.0 with 10% D_2O and 0.1 mM 4,4-dimethyl-4-silapentane-1-sulfonic acid as a shift reference. Samples contained either 50 or 100 μM β-tail (β_{1A} or β_{1D}) and different concentrations of Kindlin-3 (from 0 to 100 μM). Amide ^1H and ^{15}N resonance assignments for free β_{1A} were obtained by transferring assignments obtained previously at pH 6.1 (45). Although ^1H and ^{15}N resonance assignments at pH 6.1 were also available for free β_{1D}, the ^{15}N-HSQC spectrum at pH 7.0 was different enough to make direct transfer of all the assignments difficult. Therefore, an additional ^{15}N-HSQC of free β_{1D} was recorded at pH 6.4 to

[6] J. F. Flanagan and R. J. C. Gilbert, unpublished data.

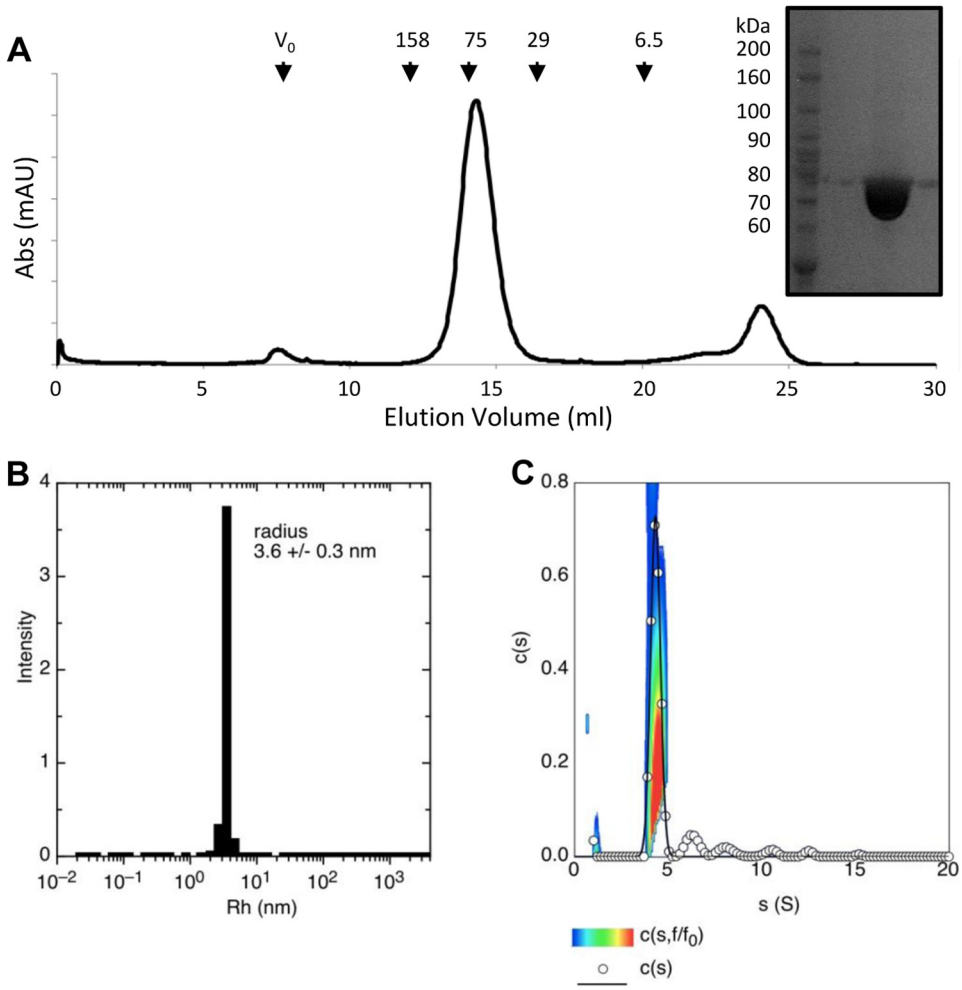

FIGURE 2. **Purification and biophysical characterization of Kindlin-3.** *A*, representative gel filtration elution profile of purified Kindlin-3 using a Superdex S200 (10/30; GE Healthcare) in Tris-HCl, pH 7.5, 150 mM NaCl, and 1 mM DTT at 20 °C. Compared with standard proteins (approximate elution volumes shown above the trace), Kindlin-3 migrates as expected for a 75-kDa protein. *B*, DLS measurements of Kindlin-3 in 20 mM Tris-HCl, pH 7.5, 100 mM NaCl, and 1 mM DTT at 22 °C. Radius estimated for a 75-kDa protein using a spherical model is 3.77 nm. *C*, $c(s,f/f_0)$ analysis of Kindlin-3 for absorbance data. The $c(s)$ (see key for *symbols*) value has a predominant species fitted with a Gaussian function, giving $s = 4.3 \pm 0.01$ S and variance (σ) $= 0.25 \pm 0.01$ S. The third dimension (see key for *contour plot*) shows the distribution of apparent weights determined by probability of frictional coefficients in the sample.

facilitate the assignment of ^{1}H and ^{15}N resonances at pH 7.0. Kindlin-induced changes in amide peak intensities of the β-tails (I/I_o) are reported as the peak height in the presence of Kindlin (I) divided by the height of the same peak in the absence of Kindlin (I_o). The interpretation of intensity changes in NMR titrations is provided in footnote below.[7]

[7] For a simple two-site exchange between tails (T) and Kindlin (K) (T + K ↔ TK), the NMR line width will change from that of T to that of TK during the titration. TK is a complex of around 80 kDa, so we would expect its line width to be much greater than that of T, which is around 6 kDa. From the observed behavior of the peaks, we believe the regime corresponds to an "intermediate" exchange, *i.e.* where the T and TK states have one averaged resonance; but even if it is the "slow" exchange regime, one peak will get smaller while retaining approximately the same line width. The reduction in intensity of the observed peak will give an indication of the affinity and specificity of the interaction whether the exchange regime is slow or intermediate. For intermediate exchange, the line width has an additional broadening term that depends on the populations of the T and TK states and the square of the shift difference between these states. This exchange contribution vanishes when the TK state dominates, but this requires a saturated TK state to be attained. We have observed cases previously (*e.g.* Ref. 47) where exchange causes line broadening that does not vanish when TK dominates, presumably because of more complex steps, such as T + K ↔ TK → TK.

RESULTS

Generation of Mouse Kindlin-3—Mouse Kindlin-3 was expressed using an insect cell expression host and recombinant baculovirus, typically yielding 5–10 mg/liter of infected insect cell culture. Standard metal affinity chromatography (IMAC) methods partially purified a ~75-kDa protein, which was further purified by anion exchange chromatography using a heparin column (see "Experimental Procedures") before a final gel filtration step that gave a homogeneous protein solution, estimated to be >95% pure by SDS-PAGE. Gel filtration (Fig. 2*A*) using Superdex S200 (10/30) (see "Experimental Procedures") exhibited a single symmetrical peak that, based on the elution volume, suggested that Kindlin-3 is predominately monomeric. Purity was further checked by tryptic digestion and liquid chromatography-mass spectroscopy/mass spectroscopy. The purified recombinant protein was thus shown to be authentic murine Kindlin-3, corresponding to UniProt accession number Q8K1B8.

Biophysical Characterization of Purified Kindlin-3—The biophysical properties of Kindlin-3 were assessed by dynamic light scattering (DLS) and AUC. DLS suggested that the protein existed

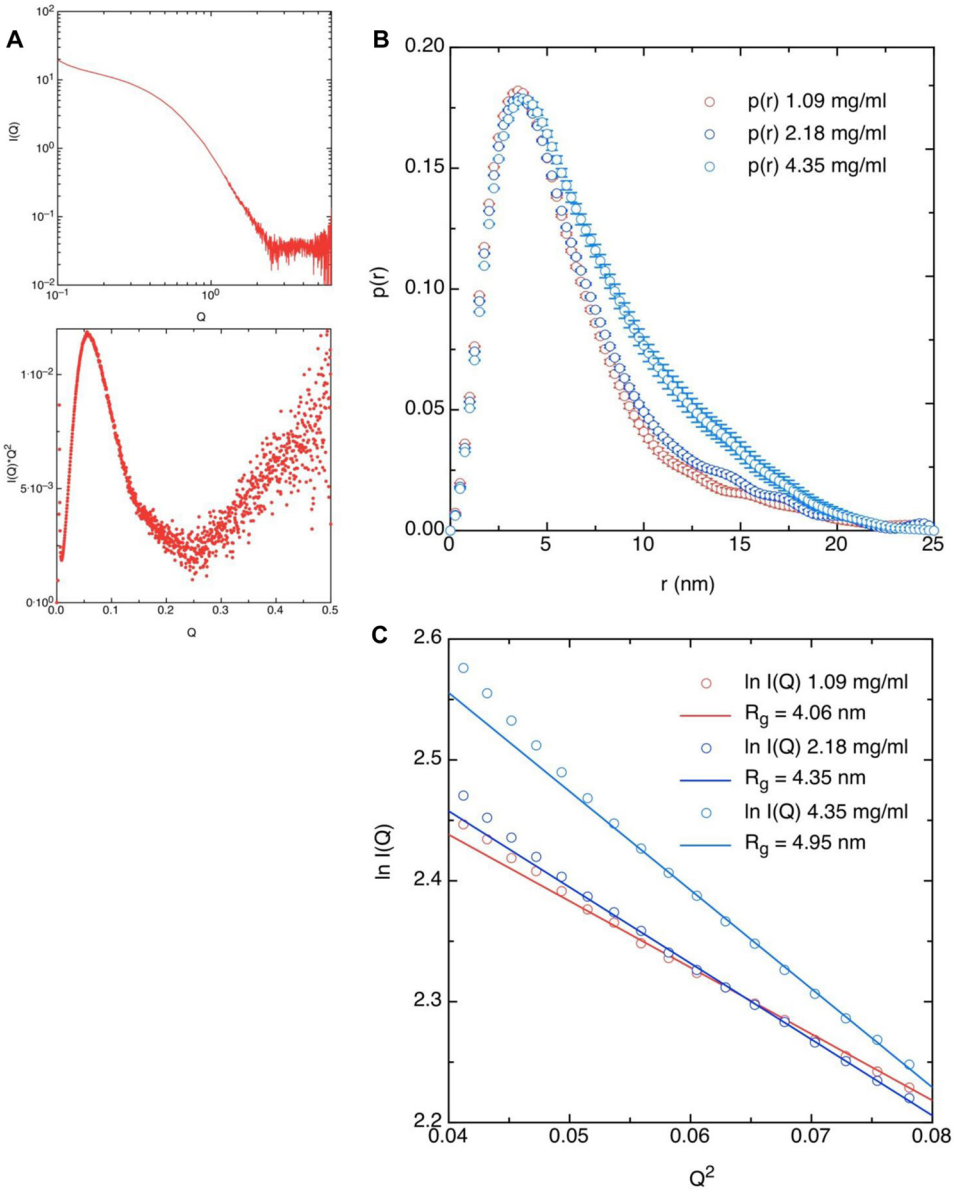

FIGURE 3. **Raw SAXS data and graphical analysis.** *A*, *I*(*Q*) scattering data for Kindlin-3 obtained at 1.09 mg/ml (*upper panel*) and their Kratky plot of $I(Q) \times Q^2$ (*lower panel*). *B*, *p*(*r*) functions computed for 1.09 mg/ml (*red symbols*), 2.18 mg/ml (*blue symbols*), and 4.35 mg/ml (*cyan symbols*). *C*, Guinier plots for the three data sets shown in *B*, colored according to the same scheme as in *B*, giving the radii of gyration shown for $Q_{max}R_g \leq 1.3$.

as a single species with a hydrodynamic radius of 3.6 nm (±0.29) (Fig. 2*B*). The insight from SEC and DLS that Kindlin-3 is predominately monomeric was underscored by AUC, where the model-independent $c(s,f/f_0)$ method of data analysis showed a single major peak with a sedimentation coefficient of 4.3 S (Fig. 2*C*). A species of 4.3 S with a weight of 75 kDa has a predicted hydrodynamic radius of 3.8 nm, in agreement with the DLS results, and a frictional coefficient of 1.46, indicating that the protein is a prolate ellipsoid with an axial ratio of 5.75 (see "Experimental Procedures" for hydrodynamic calculations). These hydrodynamic radii calculated using AUC and DLS are in excellent agreement with the 3.8-nm Stokes radius reported in Kahner *et al.* (46).

Small-angle X-ray Scattering of Kindlin-3 Reveals an Extended Conformation—SAXS data were obtained at four concentrations: 1.09, 2.18, 4.35, and 8.7 mg/ml. All four plots of *I*(*Q*) (*e.g.* Fig. 3*A*) were analyzed using the distance distribution function approach, *p*(*r*). In this method of analysis, a user-defined maximum dimension (D_{max}) for the scattering species is used to calculate a plot of rotationally averaged scattering vectors found within the particle via Fourier transformation. As the concentration of the samples increased so did the apparent D_{max}, from 14 to 20 nm, indicating the presence of some interparticle interactions (Fig. 3*B*). The two lower concentrations, however, gave very similar *p*(*r*) functions (Fig. 3*B*) with D_{max} = 14 nm and D_{max} = 16 nm (R_g 4.07 ± 0.01 and 4.51 ± 0.01, respectively). Additional Guinier analysis of the same scattering curves (Fig. 3*C*) gave radii of gyration in agreement with those from the *p*(*r*) calculation (4.06 and 4.35 nm), which validated the D_{max} determination and the conclusions made from the shape of those functions. The non-Gaussian vector length distribution of these two functions with an extended tail indicates an elongated conformation for Kindlin-3; they were thus used

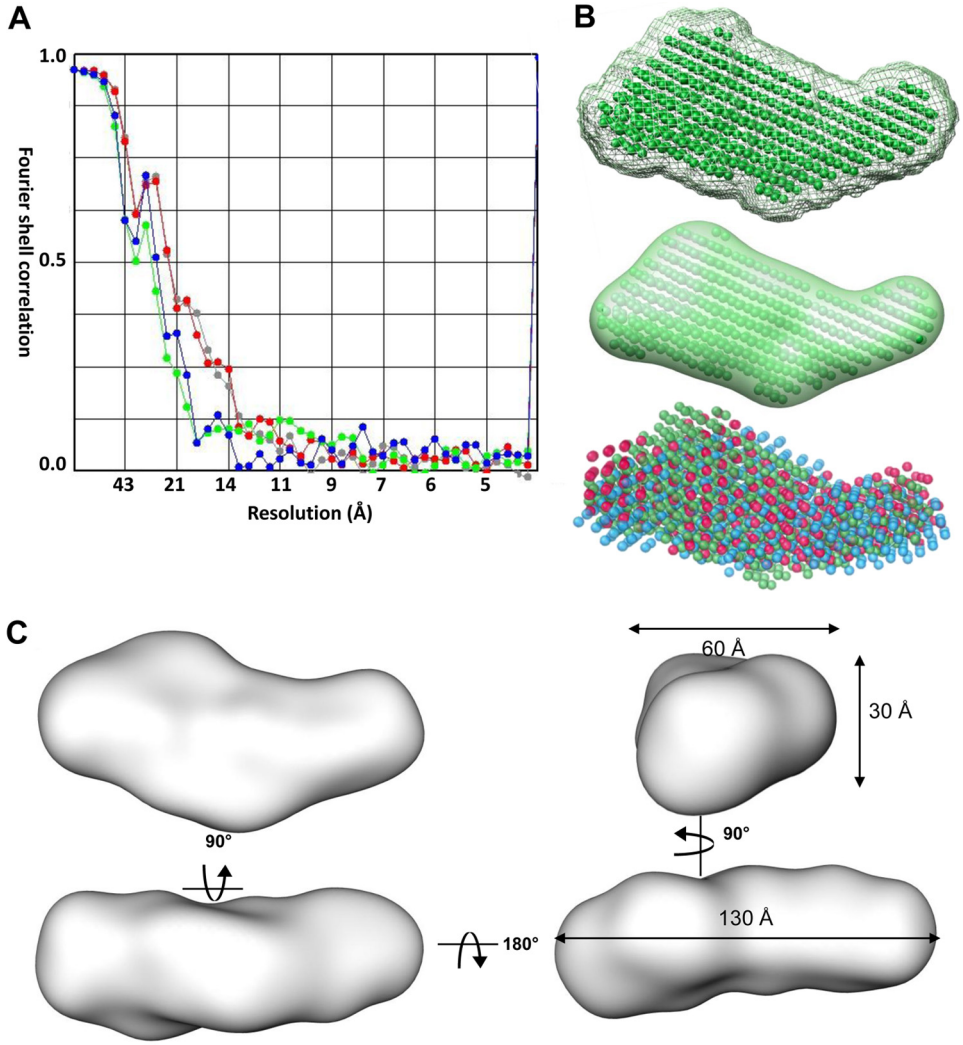

FIGURE 4. **SAXS shape reconstitution.** *A*, Fourier shell correlations (38) between independent ensembles of reconstituted scattering envelopes computed using DAMMIN. The *red* and *gray* Fourier shell correlations are for pairwise comparisons among three reconstituted models generated from data collected at the lowest two concentrations and indicate a resolution of 23 Å. These three maps were averaged and filtered to generate the consensus envelope shown in *C*. The *green* and *blue* Fourier shell correlations are for less highly correlated pairwise comparisons of ensembles of *ab initio* models, which were not included in the consensus model but indicate resolutions of 29 Å. *B*, *top*, a single DAMMIN (34, 35) model (*green dummy atoms*) obtained at 1.09 mg/ml and its envelope computed using GAP (38) (*green mesh*); shown also filtered to 29 Å resolution (*middle*). *Bottom*, superposition of the three consensus Kindlin structures agreeing with each other to 23 Å resolution; see *A* for Fourier shell correlations. *C*, orthogonal views as indicated by the rotation axes and *arrows* of the 23 Å resolution scattering envelope for Kindlin-3 generated from the consensus models shown at the bottom in *B* as described under "Experimental Procedures."

for *ab initio* shape reconstitution. By determining multiple independent ensembles of such models, we estimated the resolutions for the resulting structures to be 23–29Å using the Fourier shell correlation approach (Fig. 4*A*) (see "Experimental Procedures") (38). A representative individual ensemble consensus model, its envelope, and a filtered version at 29 Å resolution are shown in Fig. 4*B*. Three of the structures, two from data collected at the lowest concentration and one from data collected at 2.18 mg/ml, agreed with each other to a resolution of 23 Å; these (Fig. 4*B bottom*) were averaged to generate the reconstruction shown in Fig. 4*C*. As shown, the approximate overall dimensions of this envelope are 130 × 60 × 30 Å. Calculation of a theoretical sedimentation coefficient for the reconstituted envelope (see "Experimental Procedures") indicates a value of 5.0 S, in reasonable agreement with the experimental value of 4.3 S; the experimental value may be reduced by drag from the disordered loop in the F1 domain (the Kratky plot in Fig. 3*A* also suggests some disorder in the structure). The R_g of the envelope is 3.5 nm, in excellent agreement with the values determined by DLS and AUC and reported elsewhere (46). Kindlin-3 is much more elongated than the cloverleaf conformation of the radixin FERM domain but is similar in conformation to the elongated Talin head FERM domain (Fig. 5, *A* and *B*). The SAXS envelope for Kindlin-3 is, however, significantly more swollen and slightly longer than the Talin crystal structure; this is expected because of the additional domains that are absent in Talin, the 107-residue loop in the F1 subdomain and the PH domain that intersects the F2 subdomain.

We were not able to identify with certainty the position of the disordered region and the PH domain within the Kindlin-3 envelope, but we constructed various possible arrangements of the FERM subdomains and PH domain (Fig. 5*C*) constrained by two primary factors: the FERM F0-F1 and F2-F3 domains are tandems with closely interleaved folds (5) and the position of

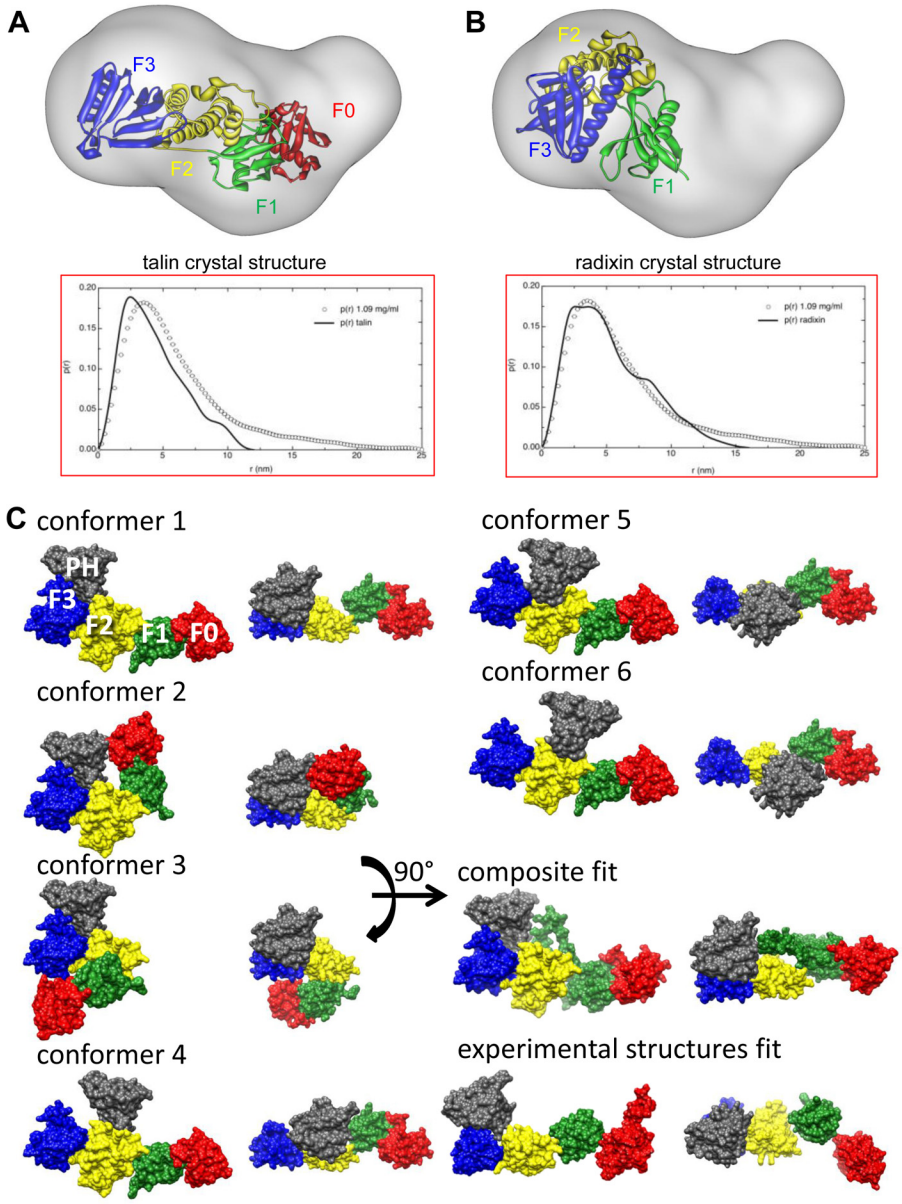

FIGURE 5. **Fitting of FERM domain structures into the Kindlin-3 SAXS envelope.** *A*, the reconstituted SAXS envelope shown in Fig. 4*C* fitted with the Talin head FERM domain (5). Domains: F0, *red*; F1, *green*; F2, *yellow*; F3, *blue*. A comparison of the crystal structure $p(r)$ curve and the experimental $p(r)$ curve determined for Kindlin-3 (Fig. 3) is shown in the *lower panel*. *B*, the SAXS envelope fitted with the radixin FERM domain (58) colored as in *A*, with the crystal structure $p(r)$ and experimental $p(r)$ shown in the *lower panel*. *C*, a series of possible arrangements (*conformers 1–6*) of the F0-F1 and F2-F3 subdomain tandems from the Talin FERM domain with respect to the Kindlin PH domain[8]; each is shown in two orthogonal views as indicated by the *arrow* of rotation. The domains are again colored as: F0, *red*; F1, *green*; F2, *yellow*; PH, *gray*; and F3, *blue*. Also shown are two alternative ways of modeling in the Kindlin domain structure: a variant of conformer 1 in which the F1 Talin subdomain (*green*) incorporates the loop region modeled in NMR data analysis (model 8 of the NMR ensemble RCSB ID 2KC2) (*composite fit*) (8); and a fit of experimental structures only, the NMR structure of Kindlin F0 (8), the crystal structures of Talin F1-F3 (5), and the crystal structure of the Kindlin-1 PH domain[8] (*experimental structures fit*). Conformer 1 and the consensus model were refined in the 23 Å scattering envelope using the program VEDA with the F0-F1 and F2-F3 tandems treated as rigid bodies; for the experimental structures fit, all five domains were treated as individual rigid bodies.

the PH domain in the polypeptide sequence. The first of these models was constructed by fitting the F0-F1 and F2-F3 domain tandems of Talin (5) and the PH domain structure from Kindlin-1[8] into the reconstituted Kindlin-3 envelope using the software VEDA (denoted *conformer 1* in Fig. 6*A*). We then assembled various alternative arrangements of the F0-F1, F2-F3, and PH domains (*conformers 2–6*) and computed scattering curves and $p(r)$ functions for conformers 1–6; these are compared with the experimental $p(r)$ profile in Fig. 6*A*. The best agreement with the experimental data is found for conformer 1 in which the PH domain sits above the F2-F3 interface. This model does not incorporate the F1 loop, but an NMR structure of the F1 subdomain of Talin alone (48) provides a model of the Talin F1 loop, although this is shorter than the Kindlin-3 loop by ~80 residues. A composite model with the F1 subdomain of the Talin crystal structure replaced by one model from the F1 NMR structure ensemble was thus constructed to indicate a

[8] L. A. Yates, C. N. Lumb, N. N. Brahme, L. E. Bird, L. De Colibus, R. J. Owens, D. A. Calderwood, M. S. P. Sansom, and R. J. C. Gilbert, submitted for publication.

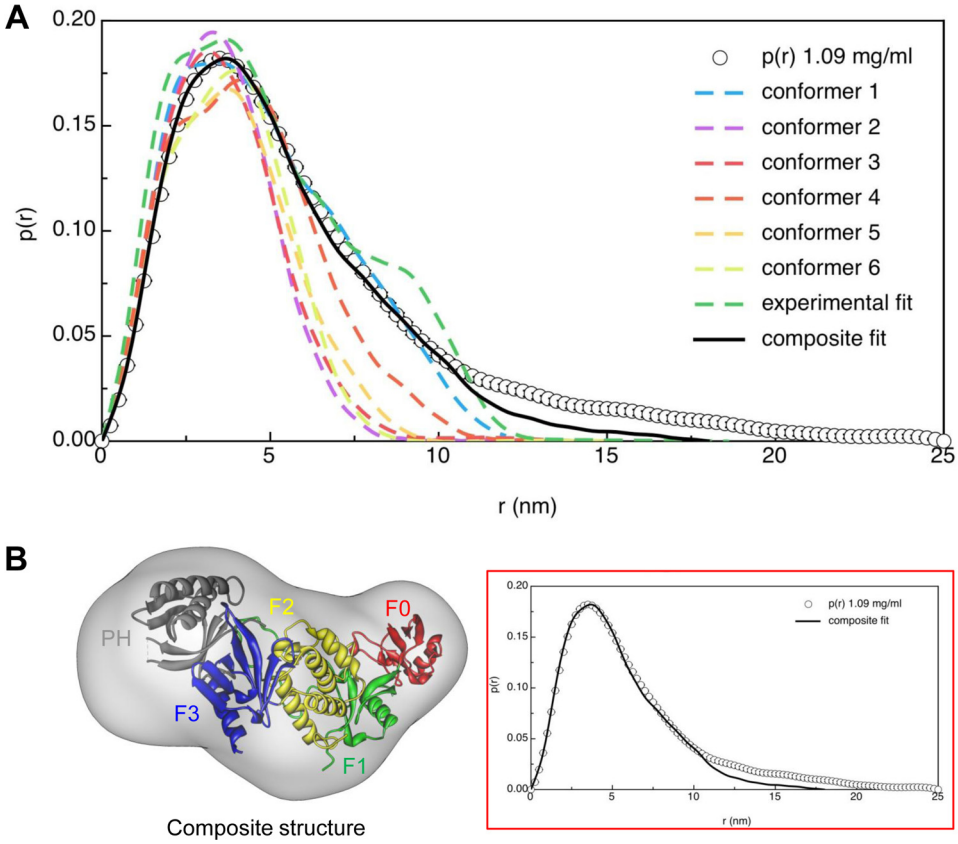

FIGURE 6. **Simulated *p*(*r*) curves consensus fit into SAXS envelope.** *A*, the experimental *p*(*r*) plot for Kindlin-3 is superimposed with *p*(*r*) calculations for each model shown in Fig. 5, according to the key. *B*, the composite fit of F0, F2, and F3 domains from the Talin crystal structure (5) with the PH domain for Kindlin-1[8] and the F1 structure including its loop (48), with the experimental *p*(*r*) and the simulation for this model shown on the *right*. See Fig. 5 for modeling and *p*(*r*) analysis of this and other models.

possible loop location in our envelope. The eighth model in the NMR ensemble was used because it was assessed as being the most probable using OLDERADO cluster analysis (49). Allowing simultaneous rigid body refinement of the composite F0-F1 tandem, the F2-F3 tandem, and the PH domain in VEDA gave an improved fit of *p*(*r*) to the experimental data (Figs. 5 and 6). This "composite model" accounts better for the long vector *p*(*r*) tail, presumably due to some account being taken of the F1 loop. The fit could probably be improved by the inclusion of additional material between the F0-F1 and F2-F3 tandems, which would take some account of the unmodeled 80 residues of the Kindlin-3 F1 loop. More detailed modeling is unjustified because of numerous unknowns, but another possible representation in which all five Kindlin subdomains (F0-F3 and PH domains) were treated as independent rigid bodies was considered. This used only crystal or NMR structures ("experimental structures fit"): the Kindlin-1 F0 domain (8), Talin F1-F3 subdomains (5), and Kindlin-1 PH domain.[8] These models were all refined in VEDA as shown in Fig. 5*C*; they too were used to compute theoretical *I*(*Q*) and thus *p*(*r*) curves (Fig. 6*A*). However their fitting did not represent an improvement over the composite model, which seems to give the best representation of the domain arrangement of Kindlin-3. This is most likely due to too many degrees of freedom when Kindlin-3 is modeled as five independent rigid bodies. Attempts to use the program SASREF (41) failed for the same reason (see "Experimental Procedures").

Interaction Partners of Kindlin-3—Heterologous interactions undergone by Kindlin-3 were assessed using SEC and AUC. SEC (Fig. 7*A*) of mixtures of Kindlin-3 (~75 kDa), integrin β_{1A} cytoplasmic tails (~6 kDa), and Talin head domain (~50 kDa) detected separated proteins, but no additional peaks were detected within the predicted elution volume range that suggested the presence of binary or ternary complexes. In the case of the β_{1A} tail complex, the expected increase in molecular weight was small, so lack of change in the SEC profile was not unexpected. Significant interactions with Talin should, however, have been readily detected if a significant amount of complex had formed under the conditions used. The concentrations of protein on SEC columns were low, however, and there was an interplay of size and shape in determining their SEC elution, so a weak interaction may not be detected.

In the case of AUC (Fig. 7*B*) we first benchmarked the apparent sedimentation behavior of Kindlin-3 and the Talin head domain alone. In anticipation of a weak interaction, we used as high a concentration of reagents as possible and thus short path length sample holders. Kindlin-3 showed a sedimentation coefficient (*s*) of 4.2 ± 0.01 S, in agreement with the value determined previously (Fig. 2*C*), and Talin head a value of 3.0 ± 0.01 S. However, the ternary mixture showed a well defined peak of $s = 3.6 \pm 0.01$ S, which indicates the formation of a (ternary) complex that, with an accumulated weight of ~130 kDa, would have a frictional coefficient of 2.51. This suggests an arrangement of Kindlin and Talin in which both interact with the integ-

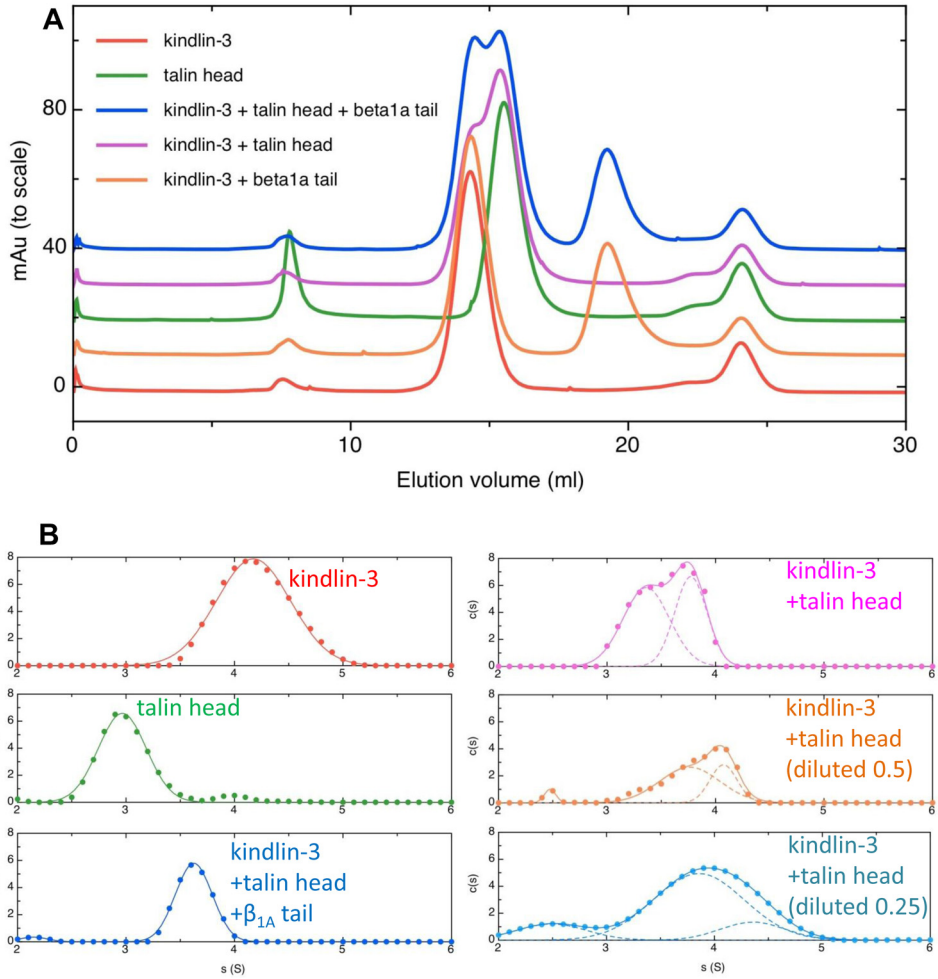

FIGURE 7. **Biophysical studies of Kindlin interactions with other proteins.** *A*, analytical SEC elution profiles of Kindlin-3 alone (*red trace*), Talin head alone (*green trace*), Kindlin-3 with Talin head and integrin β_{1A} tail (1:1:5, *blue trace*), Kindlin-3 with Talin head (1:1 molar ratio, *magenta trace*), and Kindlin-3 with integrin β_{1A} tail (1:5 molar ratio, *orange trace*). SEC was performed using 10 mM sodium phosphate, pH 7.4, 100 mM NaCl, and 1 mM DTT buffer at 20 °C. Kindlin-3 (~75 kDa) eluted at 14.4 ml, and Talin head (~50 kDa) eluted at 15.5 ml. The complex mixtures demonstrate peaks centered at 14.4 and 19.20 ml for Kindlin-3 and integrin β_{1A} tail mixed solution; 14.4, 15.4, and 19.2 ml for Kindlin-3, Talin head, and integrin β_{1A} tail mixed solution; and 14.5 and 15.4 ml for Kindlin-3 and Talin head mixed solution. All protein solutions injected were of equivalent volume (200 μl). Peaks observed at ~8 ml elution volume are in the void volume and are therefore aggregates, and peaks observed at ~24 ml elution volume represent buffer components from the protein solutions. *B*, AUC apparent sedimentation coefficient distribution (*c*(*s*)) profiles of Kindlin-3 and Talin head show that a sharp, well defined peak between Talin (3.0 S) and Kindlin-3 (4.2 S) occurs at 3.6 S, demonstrating the formation of a ternary complex with β_{1A} tails. The binary combinations of Kindlin-3 and Talin head also show the formation of an intermediate peak, suggesting that interaction occurs between the two proteins without an integrin tail, but it is a much weaker interaction and leaves substantial amounts of isolated protein that increases with dilution of the sample. These profiles are for the absorbance data collected.

rin tail simultaneously to produce an elongated conformation, *e.g.* one in which the two proteins project from opposite sides of the integrin tail, producing an assembly that is more elongated than either Talin or Kindlin alone. The conclusion that a ternary complex forms is greatly strengthened by comparing the data for the ternary mixture with those for binary combinations of Kindlin-3 and Talin. Here, a weaker interaction between Kindlin and Talin is observed such that two or three species are resolved, with a wide distribution of apparent sedimentation coefficients, indicating an exchange of molecules between associated and unassociated states. This makes the assignment of sedimentation coefficient distribution peaks to one molecular species difficult. The important point here is, however, that the large difference observed in the absence and presence of the integrin tail strongly supports the contention that β-tails promote the formation of a ternary complex. Nevertheless, the *c*(*s*) profiles of binary mixtures of Kindlin-3 and Talin head do support the existence of a binary complex, albeit one with weak affinity, as determined both from the absorbance data shown in Fig. 7*B* and from interference data (not shown).

Interaction of Kindlin-3 with β-Integrin Tails—To assess further the binding properties of our Kindlin-3 preparations, we investigated the interaction with β-tails using NMR. The tail/Kindlin-3 interaction experiments were performed at pH 6.1, in line with previous studies. ^{15}N-HSQC spectra of [U-^{15}N]β_{1A} and [U-^{15}N]β_{1D} were recorded in the presence of increasing amounts of Kindlin-3, up to a 1:1 stoichiometric ratio. Although no significant chemical shift changes were observed, the resonance intensities of several residues in both β_{1A} and β_{1D} integrin tails were suppressed by the addition of Kindlin-3 (Fig. 8*A*). The perturbed peaks mainly mapped to the previously identified membrane-distal NP*X*Y motif region (19) but also included residues associated with the Talin-specific integrin-binding motif (Fig. 8, *B* and *C*).

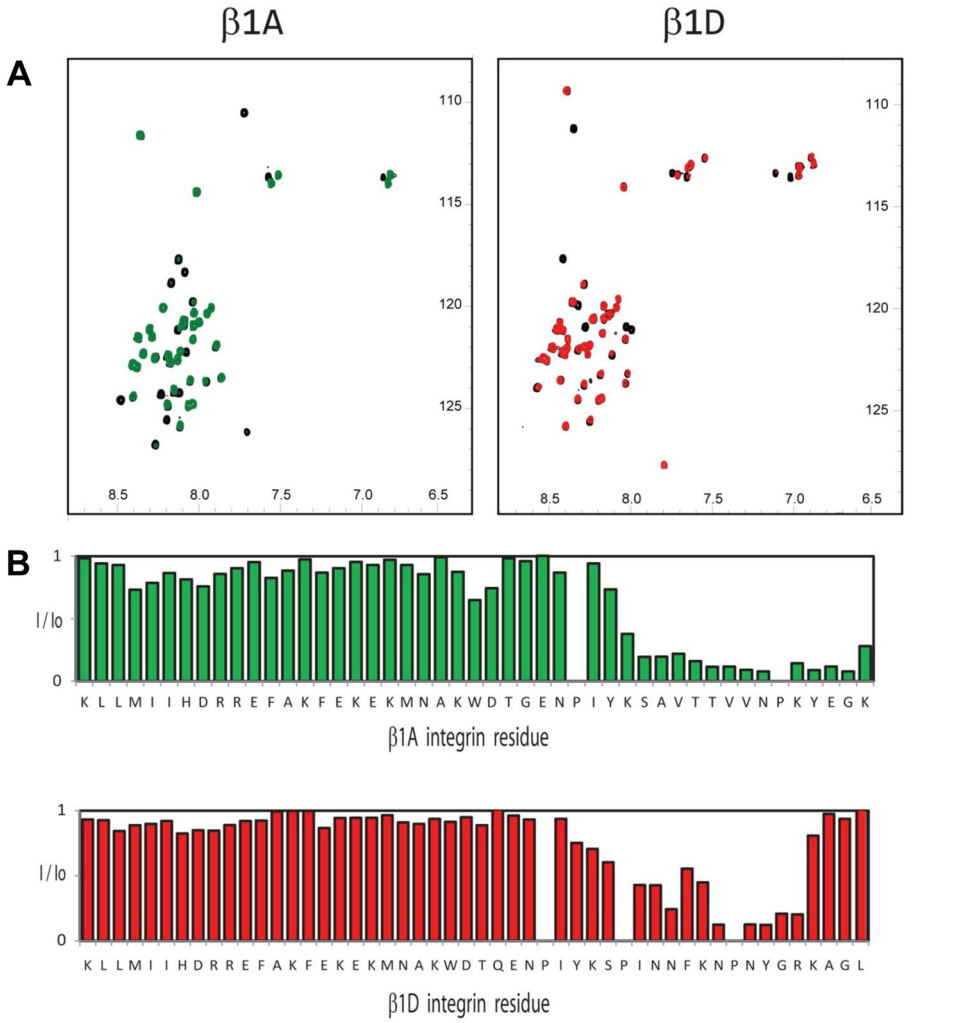

FIGURE 8. **C-terminal regions of integrin tails β_{1A} and β_{1D} interact with Kindlin-3.** *A*, ^{15}N-^{1}H HSQC spectra of 100 μM β_{1A} and β_{1D} before (*black*) and after (*green* and *red*, respectively) the addition of an equimolar amount of Kindlin-3. *B*, the intensity of specific assigned peaks, observed in *A*, plotted as an intensity ratio, I/I_o) in the presence (I) and absence (I_o) of Kindlin-3. A pronounced reduction in intensity is observed for residues in the C-terminal region of both tails, indicating a specific tail/Kindlin-3 interaction. As addition of Kindlin-3 caused some precipitation in the β_{1D} sample, β_{1D} peaks were normalized to an intense peak in the N-terminal region. *C*, sequence alignment of β_{1A} and β_{1D} integrin cytoplasmic domains. The conserved Kindlin-3 binding, highlighted in *red* and *green* as in *A* and *B*, starts immediately next to the first NP*X*Y motif (central to Talin binding, indicated in *cyan*) and includes the second NP*X*Y motif (*underlined*).

Closer inspection shows that the suppression of intensities in β_{1A} tail resonances was more marked than for the β_{1D}, suggesting a higher affinity. This is shown in detail in Fig. 9, *A* and *B*, where the peak intensity decrease is tracked as a function of Kindlin-3 concentration for equivalent residues of β_{1A} and β_{1D}. Close-ups of the HSQC spectral series show similar intensity reduction in both tails for peak Tyr-795, within the membrane-distal NP*X*Y motif, whereas Ser-785 was much less reduced in β_{1D} than in β_{1A} (Fig. 9*A*). An alternative representation is shown in Fig. 9*B*, where the intensity decrease *versus* Kindlin-3 concentration is shown also for residues Thr-788 (outside the motif) and Asn-792 (within the motif). A sequence alignment of several β-tails is shown in Fig. 10*A* in which the key features associated with their function are highlighted; the pattern of change we observed is consistent with an important role for the upstream region flanking the membrane-distal NP*X*Y motif in Kindlin binding. These results are also consistent with the previous finding that the Ser/Thr-rich region upstream of the membrane-distal NP*X*Y motif is important for modulating the strength of the interaction (19). It is not straightforward to interpret intensity changes of NMR peaks in terms of binding affinity, but the plots for Asn-792 and Tyr-795 (Fig. 9*C*) indicate a K_D of around 50 μM.

The physiological relevance of these data is underscored by the similar pattern of interactions observed during titrations performed at pH 7.0 (Figs. 10 and 11) that likewise suggests a specific interaction between Kindlin-3 and the membrane-distal NP*X*Y motifs of the β_{1A} and β_{1D} tails. Like the data obtained

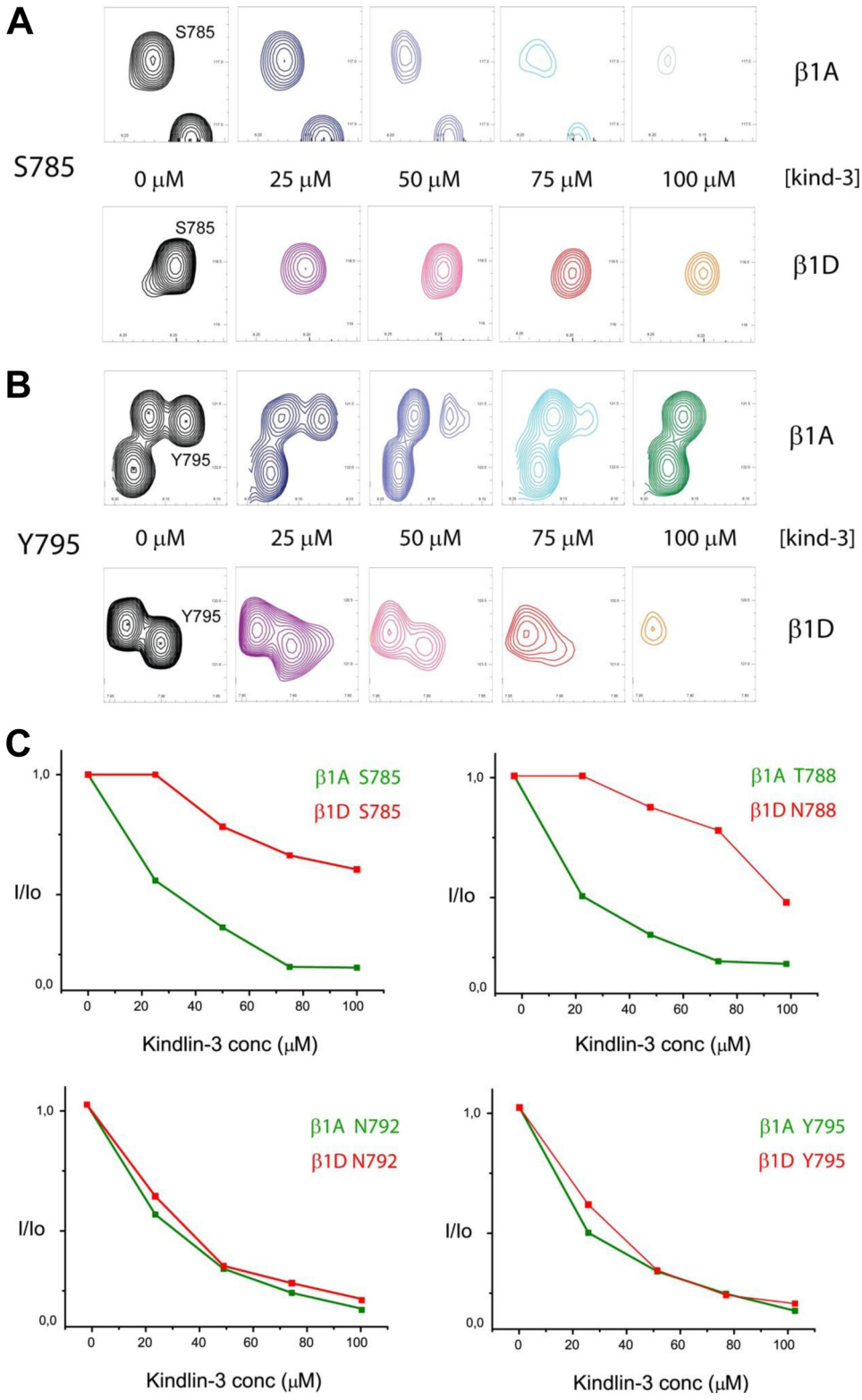

FIGURE 9. **Comparison of β_{1A} and β_{1D} binding to Kindlin-3.** *A*, snapshots of different ^{15}N-^{1}H HSQC spectra measured at increasing amounts of Kindlin-3 for the Ser-785 peak involved in Kindlin binding. A significant difference in intensity decrease is observed for Ser-785 in β_{1A} compared with β_{1D}. *B*, same as in *A* for the Tyr-795 peak also involved in Kindlin binding. The intensity decrease is greater than that for Ser-785 and almost identical for Tyr-795 in both tails, indicating the central role of the second NP*X*Y motif in the binding of Kindlin-3. *C*, plots of the observed intensity ratio at different Kindlin-3 concentrations (0, 25, 50, 75, and 100 μM) for selected β_{1A} and β_{1D} residues (*green* and *red lines*, respectively) within the Kindlin-3 binding region. Note that the intensity decrease is very similar in both tails for residues within the NP*X*Y motif (*lower plots*) but is more pronounced for residues outside the motif in β_{1A} (*upper plots*). This is consistent with the idea that the flanking regions (*e.g.* the TT sequence before the second NP*X*Y motif in β_{1A}) are important in the tail/Kindlin-3 interaction and that the overall affinity of Kindlin-3 for β_{1D} is less than for β_{1A}.

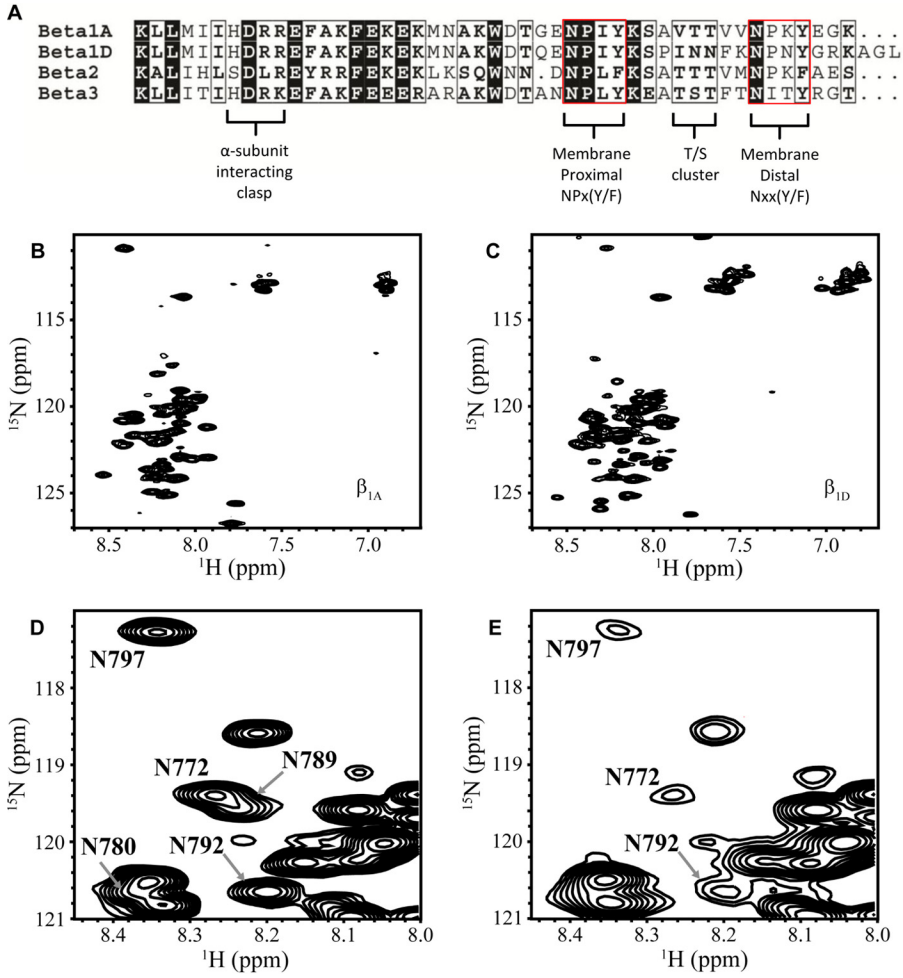

FIGURE 10. **^{15}N-HSQCs of the free β_{1A} and β_{1D} tails.** *A*, sequence alignment of four integrin β-tails in their Talin and Kindlin binding regions. *B*, a section of the β_{1A} HSQC at pH 7.0. The side chain NH peak of Trp-775 is the only peak that falls outside of the region shown here. *C*, a section of the β_{1D} HSQC at pH 7.0. The side chain NH peak of Trp-775 is the only peak that falls outside of the region shown here. *D*, a section of the β_{1D} HSQC recorded at pH 6.4, illustrating several asparagine backbone NH peaks. Peaks are labeled with their corresponding *residue number* and *single-letter amino acid code*. *E*, the same section of the HSQC recorded at pH 7.0. The backbone NH peaks of Asn-780 and Asn-789 have disappeared, whereas those of Asn-772, Asn-792, and Asn-797 have become weaker in intensity.

at pH 6.1, they point to a stronger binding of Kindlin-3 to β_{1A} than to β_{1D}. In addition, the results are again consistent with the previous observation that the Ser/Thr-rich region upstream of the NP*X*Y motif is important for modulating the strength of the interaction (19).

DISCUSSION

The Kindlin family of proteins has been the focus of much attention since their role as essential co-activators of integrins *in vivo* was discovered. This triggered a great effort to express them recombinantly and resolve their structures. To date little success has been reported with full-length proteins, but we have described here how a baculovirus system permits large scale expression at levels where structural studies become feasible. Although attempts to crystallize Kindlin-3 are ongoing, we have described here how accessory techniques can shed much light on how Kindlins act in the regulation of cell adhesion.

One possible explanation for the difficulties found in expressing recombinant fragments of Kindlins is that the normal domain arrangement is compact (*e.g.* like the domain structure of radixin) so that fragments have exposed hydrophobic surfaces. We have shown here, however, using SAXS and modeling, that murine Kindlin-3 has an elongated structure (Figs. 2–6). The best of the models constructed involved F0-F1 and F2-F3 forming the backbone of the protein with the inserted PH domain and F1 loops (Fig. 6). The demonstration that the Kindlin-3 architecture is elongated is important for the construction of models for the combined activity of Kindlins and Talin at integrin tails. One mechanistic inference from the elongated structure is that the Kindlin-3 F3 subdomain 3 could bind to the β-integrin cytoplasmic tail concomitantly with Talin, as suggested by various studies (24–26) and the AUC experiments described here (Fig. 7*B*). Another inference from the domain architecture of Kindlin-3 is that it may facilitate interactions between the PH domain and the inserted basic loop in F1 with the cytoplasmic face of the plasma membrane. This may in turn provide the correct orientation for the formation of a ternary complex with Talin and integrin β-tails, as well as an enhanced local concentration.

There is an apparent discrepancy between our solution conformation of Kindlin-3 and the very recent observation that the N- and C-terminal regions of Unc-112 (50) and, by inference,

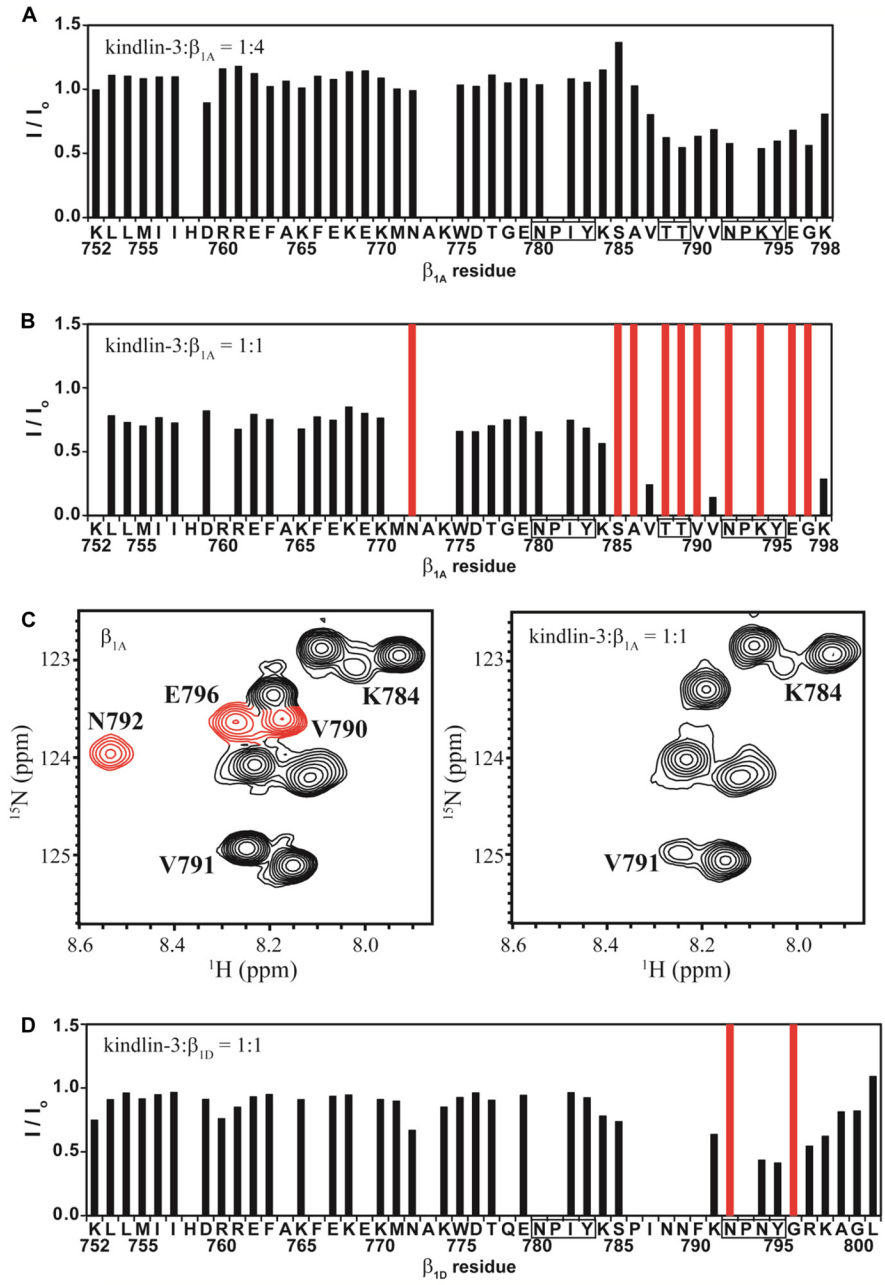

FIGURE 11. **Intensity changes in the ^{15}N-HSQC peaks of β-tails brought about by the presence of Kindlin-3.** *A*, in the presence of 0.25 molar equivalents of Kindlin-3, the peak intensities for the membrane-distal NP*X*Y motif, and the preceding Ser/Thr-rich region of β_{1A} decreased by ~50%. Here and also in *B* and *D*, Kindlin-induced changes in amide peak intensities of the β-tails (I/I_o) are reported as the peak height in the presence of Kindlin (I) divided by the height of the same peak in the absence of Kindlin (I_o). Note that the peaks from several Asn residues are weak and broad and are difficult to detect at pH 7.0, presumably because of rapid exchange with solvent water. *B*, in the presence of 1 molar equivalent of Kindlin-3, the peak intensities of the first 33 residues of β_{1A} decreased uniformly by ~25%, whereas the peak intensities of the last 14 residues disappeared completely (*red bars*) or decreased in intensity by more than 75%. *C*, close-up views of a region of the β_{1A} HSQC illustrating peak intensity changes brought about by Kindlin-3. The *left panel* shows free β_{1A}, and the *right panel* shows β_{1A} in the presence of 1 molar equivalent of Kindlin-3. Peaks experiencing large reductions in intensity are labeled with their corresponding *residue number* and *single-letter amino acid code*. In addition, peaks that disappear completely are colored *red*. *D*, in the presence of 1 molar equivalent of Kindlin-3, the peak intensities of most β_{1D} residues in the membrane-distal NP*X*Y motif and its immediate vicinity decreased by only ~50–75%, whereas the peak intensities of the remaining β_{1D} residues were approximately the same as in the free form of the tail.

the mammalian Kindlin isoforms contact each other. Further studies will be required to resolve this question, but these results might be explained if some or all of the ~100 residue loop interposed between two halves of the F1 FERM subdomain interact directly with the entire molecule.

We investigated the interactions of Kindlin-3 using analytical SEC and AUC (Fig. 7). Although SEC was unable to detect interactions between Kindlins and tails or Talin, the formation of both a ternary complex and a binary Kindlin/Talin interaction were observable by AUC. The difference in the conclusions drawn from SEC and AUC can be ascribed to several factors including perhaps most significantly the considerable dilution of the species during the analytical SEC run. SPR has recently been used to detect a ternary complex among Kindlin-2, the

Talin head, and biotinylated β_3 integrin tails attached to the chip (24). We have added here to that result by showing that the same is true for Kindlin-3 and the β_{1A} tail and that a single macromolecular assembly is formed in solution. We have also shown that a weak binary complex can form between Kindlin-3 and Talin, although a similar interaction between Kindlin-2 and Talin could not be shown by SPR or isothermal titration calorimetry (24).

Our NMR data are based on the broadening of resonances caused by Kindlin-3 binding to labeled tails. There were a number of technical challenges that had to be overcome to make these measurements, such as the production of sufficient quantities of Kindlin-3 and its stabilization at pH 6.1; but the data obtained clearly show a selective and specific interaction. NMR of the Kindlin-3/tail interaction allowed us to map the interacting residues to the membrane-distal NP*X*Y motif and adjacent Ser/Thr-rich region. Although mutation data have suggested an interaction in this region, this is the first direct, detailed biophysical evidence for the interaction. We also demonstrate that the Ser/Thr cluster adjacent to the membrane-distal NP*X*Y forms part of the actual Kindlin-tail interface. Kindlin-3 seems to undergo no significant interaction with the membrane-proximal NP*X*Y motif. NMR suggests that the interaction between Kindlin-3 and residues within the membrane-distal (MD) NP*X*Y motif is similar in both β_{1A} and β_{1D} (Fig. 7), suggesting a central role for this motif in Kindlin binding. However the interaction of Kindlin-3 with residues upstream of the MD NP*X*Y motif is significantly greater for β_{1A} than for β_{1D}, suggesting that the context of the NP*X*Y motifs influences the overall binding affinity. Because the β_{1D} tail lacks the Ser/Thr cluster (see sequences in Fig. 9*C*), these data are consistent with those recently reported for Kindlin-2 binding to β_1 and β_3 tails, where the same extended recognition patch, including the Ser/Thr cluster, was identified (19, 24).

The conversion of integrins from a bent, low-affinity state, to an extended intermediate/high-affinity state, and their relationship to β-tail binding by Talin and Kindlin-3, has recently been investigated in rolling and arrested murine neutrophils. Talin binding to β-integrin tails in $\alpha_L\beta_2$ induced an extended/closed headpiece, a putative intermediate affinity state found in neutrophil slow rolling (25). Both Talin-1 and Kindlin-3 were, however, required for induction of the high-affinity conformation of $\alpha_L\beta_2$, which results in neutrophil arrest. These results suggested that Kindlin and Talin have distinct roles in the activation of $\alpha_L\beta_2$.

Kindlins have been shown to be involved in both inside-out and outside-in integrin signaling (12). Recently, a Kindlin-3·RACK1·β_2 integrin ternary complex associated with outside-in signaling was described (51). Investigations using platelets, where Kindlin-3 is expressed selectively, have demonstrated that outside-in signaling involves residues within the Kindlin-3 binding site that we have mapped (13), in particular threonines 788 and 789 in β_{1A} (12).

Phosphorylation of the cytoplasmic tails of β-integrins is considered a regulatory switch in their signaling, as this alters the affinity of the adaptor proteins that associate with the β-tail (52). The tyrosines from both NP*X*Y motifs in β-tails can be phosphorylated, and it has been demonstrated that phosphorylation of the MP NP*X*Y of β_3 promotes the binding of Dok1, a negative regulator of integrin activation, over Talin (29) and that phosphorylation of the MD NP*X*Y in β_3 inhibits the binding of Kindlin-2 (53). However, the consequence of tyrosine phosphorylation at the NP*X*Y motifs seems to be integrin-specific, with mice that possess a double tyrosine-to-phenylalanine mutation in β_1-tails presenting no disease phenotype (54), whereas the same mutations made in β_3 results in a bleeding phenotype (55).

In addition to tyrosine phosphorylation of the two NP*X*Y motifs, serine and threonine residues within the intervening sequence can also be phosphorylated (52). As the Kindlin binding site encompasses the serine/threonine-rich region between the NP*X*Y motifs, it is likely that phosphorylation of these residues alters Kindlin binding. Studying the effect of tyrosine and/or serine/threonine phosphorylation is beyond the scope of this article, but it is highly likely to influence Kindlin binding. Irrespective of the phosphorylation state of the β-tail threonines, it must be noted that the intervening threonines between the NP*X*Y motifs in the Kindlin-binding site of β_{1A} are critical for integrin function and trafficking, with T788A/T789A substitutions in β_1 resulting in defective integrin turnover and degradation (56). Additionally it has been demonstrated that the MD NP*X*Y motif is involved in integrin internalization and recycling (56, 26). Depletion of Kindlin-2 increases degradation of $\alpha_5\beta_1$ integrin (26) and sorting Nexin 17 (SNX17) inhibits lysosomal degradation by binding and displacing Kindlin from the Kindlin-binding site (56).

The Kindlin family of proteins has been, and will continue to be, a focus of attention because of their critical role in integrin activation and focal adhesion assembly. By generating sufficient quantities of recombinant Kindlin-3, using a baculovirus expression system we have been able to provide the first structural insight into a full-length Kindlin conformation and to define binary and ternary interactions involving integrin tails. These investigations will help in the construction of models that describe how Talin and Kindlins cooperate to form a quaternary complex with β-tails and the cytoplasmic face of the membrane to promote integrin activation.

Acknowledgments—We thank Dr. Michèle Erat for assistance with the SAXS data collection. The Oxford Division of Structural Biology is part of the Wellcome Trust Centre for Human Genetics (Wellcome Trust Core Award Grant 090532/Z/09/Z).

REFERENCES

1. Hynes, R. O. (2002) Integrins: bidirectional, allosteric signaling machines. *Cell* **110,** 673–687
2. Anthis, N. J., and Campbell, I. D. (2011) The tail of integrin activation. *Trends Biochem. Sci.* **36,** 191–198
3. Kim, C., Ye, F., and Ginsberg, M. H. (2011) Regulation of integrin activation. *Annu. Rev. Cell Dev. Biol.* **27,** 321–345
4. Moser, M., Legate, K. R., Zent, R., and Fässler, R. (2009) The tail of integrins, Talin, and Kindlins. *Science* **324,** 895–899
5. Elliott, P. R., Goult, B. T., Kopp, P. M., Bate, N., Grossmann, J. G., Roberts, G. C., Critchley, D. R., and Barsukov, I. L. (2010) The Structure of the Talin head reveals a novel extended conformation of the FERM domain. *Structure* **18,** 1289–1299
6. Meves, A., Stremmel, C., Gottschalk, K., and Fässler, R. (2009) The Kindlin

protein family: new members to the club of focal adhesion proteins. *Trends Cell Biol.* **19,** 504–513
7. Siegel, D. H., Ashton, G. H., Penagos, H. G., Lee, J. V., Feiler, H. S., Wilhelmsen, K. C., South, A. P., Smith, F. J., Prescott, A. R., Wessagowit, V., Oyama, N., Akiyama, M., Al Aboud, D., Al Aboud, K., Al Githami, A., Al Hawsawi, K., Al Ismaily, A., Al-Suwaid, R., Atherton, D. J., Caputo, R., Fine, J. D., Frieden, I. J., Fuchs, E., Haber, R. M., Harada, T., Kitajima, Y., Mallory, S. B., Ogawa, H., Sahin, S., Shimizu, H., Suga, Y., Tadini, G., Tsuchiya, K., Wiebe, C. B., Wojnarowska, F., Zaghloul, A. B., Hamada, T., Mallipeddi, R., Eady, R. A., McLean, W. H., McGrath, J. A., and Epstein, E. H. (2003) Loss of Kindlin-1, a human homolog of the *Caenorhabditis elegans* actin-extracellular matrix linker protein UNC-112, causes Kindler syndrome. *Am. J. Hum. Genet.* **73,** 174–187
8. Goult, B. T., Bouaouina, M., Harburger, D. S., Bate, N., Patel, B., Anthis, N. J., Campbell, I. D., Calderwood, D. A., Barsukov, I. L., Roberts, G. C., and Critchley, D. R. (2009) The structure of the N terminus of Kindlin-1: a domain important αiibβ3 integrin activation. *J. Mol. Biol.* **394,** 944–956
9. Ussar, S., Wang, H. V., Linder, S., Fässler, R., and Moser, M. (2006) The Kindlins: subcellular localization and expression during murine development. *Exp. Cell Res.* **312,** 3142–3151
10. Bialkowska, K., Ma, Y. Q., Bledzka, K., Sossey-Alaoui, K., Izem, L., Zhang, X., Malinin, N., Qin, J., Byzova, T., and Plow, E. F. (2010) The integrin co-activator Kindlin-3 is expressed and functional in a non-hematopoietic cell, the endothelial cell. *J. Biol. Chem.* **285,** 18640–18649
11. Boyd, R. S., Adam, P. J., Patel, S., Loader, J. A., Berry, J., Redpath, N. T., Poyser, H. R., Fletcher, G. C., Burgess, N. A., Stamps, A. C., Hudson, L., Smith, P., Griffiths, M., Willis, T. G., Karran, E. L., Oscier, D. G., Catovsky, D., Terrett, J. A., and Dyer, M. J. (2003) Proteomic analysis of the cell-surface membrane in chronic lymphocytic leukemia: identification of two novel proteins, BCNP1 and MIG2B. *Leukemia* **17,** 1605–1612
12. Moser, M., Bauer, M., Schmid, S., Ruppert, R., Schmidt, S., Sixt, M., Wang, H. V., Sperandio, M., and Fässler, R. (2009) Kindlin-3 is required for β2 integrin-mediated leukocyte adhesion to endothelial cells. *Nat. Med.* **15,** 300–305
13. Moser, M., Nieswandt, B., Ussar, S., Pozgajova, M., and Fässler, R. (2008) Kindlin-3 is essential for integrin activation and platelet aggregation. *Nat. Med.* **14,** 325–330
14. Schmidt, S., Nakchbandi, I., Ruppert, R., Kawelke, N., Hess, M. W., Pfaller, K., Jurdic, P., Fässler, R., and Moser, M. (2011) Kindlin-3-mediated signaling from multiple integrin classes is required for osteoclast-mediated bone resorption. *J. Cell Biol.* **192,** 883–897
15. Malinin, N. L., Zhang, L., Choi, J., Ciocea, A., Razorenova, O., Ma, Y. Q., Podrez, E. A., Tosi, M., Lennon, D. P., Caplan, A. I., Shurin, S. B., Plow, E. F., and Byzova, T. V. (2009) A point mutation in KINDLIN3 ablates activation of three integrin subfamilies in humans. *Nat. Med.* **15,** 313–318
16. Krüger, M., Moser, M., Ussar, S., Thievessen, I., Luber, C. A., Forner, F., Schmidt, S., Zanivan, S., Fässler, R., and Mann, M. (2008) SILAC mouse for quantitative proteomics uncovers Kindlin-3 as an essential factor for red blood cell function. *Cell* **134,** 353–364
17. Anthis, N. J., Wegener, K. L., Critchley, D. R., and Campbell, I. D. (2010) Structural diversity in integrin/Talin interactions. *Structure* **18,** 1654–1666
18. Wegener, K. L., Partridge, A. W., Han, J., Pickford, A. R., Liddington, R. C., Ginsberg, M. H., and Campbell, I. D. (2007) Structural basis of integrin activation by Talin. *Cell* **128,** 171–182
19. Harburger, D. S., Bouaouina, M., and Calderwood, D. A. (2009) Kindlin-1 and -2 directly bind the C-terminal region of β-integrin cytoplasmic tails and exert integrin-specific activation effects. *J. Biol. Chem.* **284,** 11485–11497
20. Has, C., Herz, C., Zimina, E., Qu, H. Y., He, Y., Zhang, Z. G., Wen, T. T., Gache, Y., Aumailley, M., and Bruckner-Tuderman, L. (2009) Kindlin-1 Is required for RhoGTPase-mediated lamellipodia formation in keratinocytes. *Am. J. Pathol.* **175,** 1442–1452
21. Kloeker, S., Major, M. B., Calderwood, D. A., Ginsberg, M. H., Jones, D. A., and Beckerle, M. C. (2004) The Kindler syndrome protein is regulated by transforming growth factor-β and involved in integrin-mediated adhesion. *J. Biol. Chem.* **279,** 6824–6833
22. Ma, Y. Q., Qin, J., Wu, C., and Plow, E. F. (2008) Kindlin-2 (Mig-2): a co-activator of β3 integrins. *J. Cell Biol.* **181,** 439–446
23. Montanez, E., Ussar, S., Schifferer, M., Bösl, M., Zent, R., Moser, M., and Fässler, R. (2008) Kindlin-2 controls bidirectional signaling of integrins. *Genes Dev.* **22,** 1325–1330
24. Bledzka, K., Liu, J., Xu, Z., Perera, H. D., Yadav, S. P., Bialkowska, K., Qin, J., Ma, Y. Q., and Plow, E. F. (2012) Spatial coordination of Kindlin-2 with Talin head domain in interaction with integrin β cytoplasmic tails. *J. Biol. Chem.* **287,** 24585–24594
25. Lefort, C. T., Rossaint, J., Moser, M., Petrich, B. G., Zarbock, A., Monkley, S. J., Critchley, D. R., Ginsberg, M. H., Fässler, R., and Ley, K. (2012) Distinct roles for Talin-1 and Kindlin-3 in LFA-1 extension and affinity regulation. *Blood* **119,** 4275–4282
26. Margadant, C., Kreft, M., de Groot, D. J., Norman, J. C., and Sonnenberg, A. (2012) Distinct roles of Talin and Kindlin in regulating integrin α5β1 function and trafficking. *Curr. Biol.* **22,** 1554–1563
27. Berrow, N. S., Alderton, D., Sainsbury, S., Nettleship, J., Assenberg, R., Rahman, N., Stuart, D. I., and Owens, R. J. (2007) A versatile ligation-independent cloning method suitable for high-throughput expression screening applications. *Nucleic Acids Res.* **35,** e45
28. Merrington, C. L., Bailey, M. J., and Possee, R. D. (1997) Manipulation of baculovirus vectors. *Mol. Biotechnol.* **8,** 283–297
29. Oxley, C. L., Anthis, N. J., Lowe, E. D., Vakonakis, I., Campbell, I. D., and Wegener, K. L. (2008) An integrin phosphorylation switch: the effect of β3 integrin tail phosphorylation on Dok1 and Talin binding. *J. Biol. Chem.* **283,** 5420–5426
30. Brown, P. H., and Schuck, P. (2006) Macromolecular size-and-shape distributions by sedimentation velocity analytical ultracentrifugation. *Biophys. J.* **90,** 4651–4661
31. Roessle, M. W., Klaering, R., Ristau, U., Robrahn, B., Jahn, D., Gehrmann, T., Konarev, P., Round, A., Fiedler, S., Hermes, C., and Svergun, D. I. (2007) Upgrade of the small-angle X-ray scattering beamline X33 at the European Molecular Biology Laboratory, Hamburg. *J. Appl. Crystallogr.* **40,** S190–S194
32. Konarev, P., Volkov, V. V., Sokolova, A. V., Koch, M. H., and Svergun, D. I. (2003) A Windows PC-based system for small-angle scattering data analysis. *J. Appl. Crystallogr.* **36,** 1277–1282
33. Svergun, D. I. (1992) Determination of the regularization parameter in indirect-transform methods using perceptual criteria. *J. Appl. Crystallogr.* **25,** 495–503
34. Svergun, D. I., Petoukhov, M. V., and Koch, M. H. (2001) Determination of domain structure of proteins from X-ray solution scattering. *Biophys. J.* **80,** 2946–2953
35. Volkov, V. V., and Svergun, D. I. (2003) Uniqueness of *ab initio* shape determination in small-angle scattering. *J. Appl. Crystallogr.* **36,** 860–864
36. Pettersen, E. F., Goddard, T. D., Huang, C. C., Couch, G. S., Greenblatt, D. M., Meng, E. C., and Ferrin, T. E. (2004) UCSF chimera: a visualization system for exploratory research and analysis. *J. Comput. Chem.* **25,** 1605–1612
37. Grimes, J. M., Burroughs, J. N., Gouet, P., Diprose, J. M., Malby, R., Ziéntara, S., Mertens, P. P., and Stuart, D. I. (1998) The atomic structure of the bluetongue virus core. *Nature* **395,** 470–478
38. Grigorieff, N. (2000) Resolution measurement in structures derived from single particles. *Acta Crystallogr. D Biol. Crystallogr.* **56,** 1270–1277
39. de la Torre, J. G., Echenique Gdel, R., and Ortega, A. (2007) Improved calculation of rotational diffusion and intrinsic viscosity of bead models for macromolecules and nanoparticles. *J. Phys. Chem. B* **111,** 955–961
40. Kratky, O., Porod, G., and Kahovec, L. (1951) Einige Neuerungen in der Technik und Auswertung von Röntgen-Kleinwinkelmessungen. *Z. Elektrochem.* **55,** 53–59
41. Petoukhov, M. V., and Svergun, D. I. (2005) Global rigid body modeling of macromolecular complexes against small-angle scattering data. *Biophys. J.* **89,** 1237–1250
42. Delaglio, F., Grzesiek, S., Vuister, G. W., Zhu, G., Pfeifer, J., and Bax, A. (1995) NMRPipe: a multidimensional spectral processing system based on UNIX pipes. *J. Biomol. NMR* **6,** 277–293
43. Goddard, T. D., and Kneller, D. G. (2000) *SPARKY 3*, University of California, San Francisco
44. Vranken, W. F., Boucher, W., Stevens, T. J., Fogh, R. H., Pajon, A., Llinas,

M., Ulrich, E. L., Markley, J. L., Ionides, J., and Laue, E. D. (2005) The CCPN data model for NMR spectroscopy: development of a software pipeline. *Proteins* **59,** 687–696

45. Anthis, N. J., Wegener, K. L., Ye, F., Kim, C., Goult, B. T., Lowe, E. D., Vakonakis, I., Bate, N., Critchley, D. R., Ginsberg, M. H., and Campbell, I. D. (2009) The structure of an integrin/Talin complex reveals the basis of inside-out signal transduction. *EMBO J.* **28,** 3623–3632
46. Kahner, B. N., Kato, H., Banno, A., Ginsberg, M. H., Shattil, S. J., and Ye, F. (2012) Kindlins, integrin activation, and the regulation of Talin recruitment to αIIbβ3. *PLoS One* **7,** e34056
47. García-Alvarez, B., de Pereda, J. M., Calderwood, D. A., Ulmer, T. S., Critchley, D., Campbell, I. D., Ginsberg, M. H., and Liddington, R. C. (2003) Structural determinants of integrin recognition by Talin. *Mol. Cell* **11,** 49–58
48. Goult, B. T., Bouaouina, M., Elliott, P. R., Bate, N., Patel, B., Gingras, A. R., Grossmann, J. G., Roberts, G. C., Calderwood, D. A., Critchley, D. R., and Barsukov, I. L. (2010) Structure of a double ubiquitin-like domain in the Talin head: a role in integrin activation. *EMBO J.* **29,** 1069–1080
49. Kelley, L. A., and Sutcliffe, M. J. (1997) OLDERADO: on-line database of ensemble representatives and domains. *Protein Sci.* **6,** 2628–2630
50. Qadota, H., Moerman, D. G., and Benian, G. M. (2012) A Molecular mechanism for the requirement of PAT-4 (integrin-linked kinase (ILK)) for the localization of UNC-112 (Kindlin) to integrin adhesion sites. *J. Biol. Chem.* **287,** 28537–28551
51. Feng, C., Li, Y. F., Yau, Y. H., Lee, H. S., Tang, X. Y., Xue, Z. H., Zhou, Y. C., Lim, W. M., Cornvik, T. C., Ruedl, C., Shochat, S. G., and Tan, S. M. (2012) Kindlin-3 mediates integrin αLβ2 outside-in signaling, and it interacts with scaffold protein receptor for activated-C kinase 1 (RACK1). *J. Biol. Chem.* **287,** 10714–10726
52. Legate, K. R., and Fässler, R. (2009) Mechanisms that regulate adaptor binding to β-integrin cytoplasmic tails. *J. Cell Sci.* **122,** 187–198
53. Bledzka, K., Bialkowska, K., Nie, H., Qin, J., Byzova, T., Wu, C., Plow, E. F., and Ma, Y. Q. (2010) Tyrosine phosphorylation of integrin β3 regulates Kindlin-2 binding and integrin activation. *J. Biol. Chem.* **285,** 30370–30374
54. Czuchra, A., Meyer, H., Legate, K. R., Brakebusch, C., and Fässler, R. (2006) Genetic analysis of beta1 integrin "activation motifs" in mice. *J. Cell Biol.* **174,** 889–899
55. Law, D. A., DeGuzman, F. R., Heiser, P., Ministri-Madrid, K., Killeen, N., and Phillips, D. R. (1999) Integrin cytoplasmic tyrosine motif is required for outside-in αIIbβ3 signalling and platelet function. *Nature* **401,** 808–811
56. Böttcher, R. T., Stremmel, C., Meves, A., Meyer, H., Widmaier, M., Tseng, H. Y., and Fässler, R. (2012) Sorting Nexin 17 prevents lysosomal degradation of β1 integrins by binding to the β1-integrin tail. *Nat. Cell Biol.* **14,** 584–592
57. Gouet, P., Courcelle, E., Stuart, D. I., and Métoz, F. (1999) ESPript: analysis of multiple sequence alignments in PostScript. *Bioinformatics* **15,** 305–308
58. Mori, T., Kitano, K., Terawaki, S., Maesaki, R., Fukami, Y., and Hakoshima, T. (2008) Structural basis for CD44 recognition by ERM proteins. *J. Biol. Chem.* **283,** 29602–29612